TAMPEREEN TEKNILLINEN YLIOPISTO
TAMPERE UNIVERSITY OF TECHNOLOGY

OSSI TUOMINEN

ENHANCING NONLINEAR OPTICAL RESPONSE OF RESONANT GOLD NANOSTRUCTURES VIA LATTICE INTERACTIONS

Master of Science Thesis

Examiners: Dr. Robert Czaplicki
and Prof. Martti Kauranen
Examiners and topic approved
on January 31st 2018

ABSTRACT

OSSI TUOMINEN: Enhancing nonlinear optical response of resonant gold nanostructures via lattice interactions
Tampere University of Technology
Master of Science Thesis, 49 pages
February 2018
Degree programme of Science and Engineering
Major subject: Advanced engineering physics
Examiners: Dr. Robert Czaplicki and Prof. Martti Kauranen
Keywords: gold nanostructures, resonance enhancement, surface lattice resonances

Metal nanostructures are of interest because of their potential applications in optical metamaterials, which are artificial materials that can have physical properties not found in nature. Such nanostructures are also interesting for nonlinear optics, because they can be manufactured for the desired symmetries for specific nonlinear effects, and because the presence of plasmon resonances can greatly enhance the nonlinear responses. Additionally, surface lattice resonances (SLR), arising from coupling between particles, can further modify the response.

In this work, the optical properties of metamaterials consisting of arrays of L-shaped gold nanoparticles of different sizes are studied. The nanoparticles are organised in square lattices with different dimensions of the unit cells and orientations of the particles in the array. Variation of such parameters allows to obtain structures supporting SLRs at different wavelengths. The linear properties of the structures are studied using extinction spectrometry and the nonlinear optical properties by measuring second-harmonic generation (SHG).

The results presented in this work provide strong evidence for the importance of SLRs. The measured extinction spectra show that presence of SLR near a plasmon resonance leads to an improvement of the quality of the resonance, which increases the SHG response via boosted resonance enhancement. However, due to an oversight in the design of the extinction setup, typical spectral features of SLRs were not observed, and conclusive results could not be achieved. The results are still promising, and the effects of SLRs warrant further studies.

TIIVISTELMÄ

OSSI TUOMINEN: Kultananorakenteiden epälineaarisen vasteen vahvistaminen hilavuorovaikutusten avulla
Tampereen Teknillinen Yliopisto
Diplomityö, 49 sivua
Helmikuu 2018
Teknis-luonnontieteellinen koulutusohjelma
Pääaine: Teknillinen fysiikka
Tarkastajat: Tri. Robert Czaplicki ja Prof. Martti Kauranen
Avainsanat: kultananorakenteet, plasmoniresonanssi, hilaresonanssi

Metallinanorakenteet ovat kiinnostava tutkimuskohde, koska niitä voidaan hyödyntää optisisten metamateriaalien valmistamisessa. Optiset metamateriaalit ovat keinotekoisia materiaaleja, joilla on fysikaalisia ominaisuuksia, joita ei havaita luonnollisissa materiaaleissa. Metallinanorakenteita voidaan käyttää myös epälineaarisessa optiikassa, jossa rakenteiden räätälöitävyys mahdollistaa haluttujen symmetriaominaisuuksien saavuttamiseksi. Lisäksi rakenteiden plasmoniresonanssit vahvistavat niiden epälineaarista vastetta, ja hilavuorovaikutusten avulla optista vastetta voidaan muokata edelleen.

Tässä työssä tutkittiin metallinanorakenteita, jotka koostuvat säännöllisiin hiloihin järjestetyistä L-muotoisista kultananohiukkasista. Hiukkasten ja hilojen yksikkösolun kokoa ja asentoa muuteltiin eri rakenteiden välillä, mikä johti hila- ja plasmoniresonansseihin eri aallonpituuksilla. Rakenteiden lineaarisia ominaisuuksia tutkittiin ekstinktiospektrien ja epälineaarisia ominaisuuksia taajuudenkahdennuksen avulla.

Tulosten perusteella hilaresonansseilla on merkittävä vaikutus nanorakenteiden optiseen vasteeseen. Mitatuista ekstinktiospektreistä havaitaan, että plasmoni- ja hilaresonanssien ollessa lähekkäin rakenteen resonanssin laatu paranee, mikä johtaa taajuudenkahdennusilmiön voimistumiseen. Spektrometrin suunnittelussa tehdyn virheen vuoksi kaikkia hilaresonansseille tyypillisiä spektrin yksityiskohtia ei kuitenkaan havaittu. Tämän vuoksi kattavia lopullisia johtopäätöksiä ei voitu tehdä. Tästä huolimatta tulokset olivat rohkaisevia ja lisätutkimusta hilaresonanssien ymmärtämiseksi suositellaan.

PREFACE

This Thesis was done in the Nonlinear Optics Group of the Laboratory of Photonics of Tampere University of Technology under the guidance of Doctor Robert Czaplicki and Professor Martti Kauranen. The experimental work was carried out between September 2016 and June 2017, and the writing of the Thesis took place between autumn 2017 and early 2018.

First and foremost, I want to thank my examiners for all their feedback and advice. I cannot stress enough how important and helpful all of it was for me. Also thanks to Doctor Ismo Vartiainen for manufacturing the samples studied in this work. I also have to mention Timo and Antti for their help with the experimental setups.

I also want to extend my thanks to everyone in the Laboratory of Photonics, as working alongside you was one of the best experiences in my life. Also, special thanks to Joona, who has been a great friend over our years at TUT.

Thanks to my mother Tuula, father Olli, and sister Anna, for all the support I have received over the years. Finally, last but not least, my wife Johanna: for everything.

Tampere 22.1.2018
Ossi Tuominen

CONTENTS

LIST OF ABBREVIATIONS AND SYMBOLS

Vector quantities are written in **bold** and scalar quantities in *italics*.

$\mathbf{A}$	Complex amplitude
A	Nonlinear response tensor
A_{ijk}	Nonlinear response tensor component ijk
a	Nonlinear restoring force parameter
$\mathbf{B}$	Magnetic flux density
c	Speed of light
c.c.	Complex conjugate
$\mathbf{D}$	Electric displacement field
D	Denominator function
d	Dipole moment
$\mathbf{E}$	Electric field
E	Electric field
F	Force
e	The elementary charge
f	Frequency
$\mathbf{H}$	Magnetic field
h	Planck constant
$\hbar$	Reduced Planck constant
$\mathbf{J}$	Free current density
$\mathbf{k}$	Wave vector
k	Wavenumber
k_{ij}	Resonance mode wavenumber
l	Arm length of the nanoparticle
$\mathbf{M}$	Magnetisation
m	Mass
N	Number density
n	Index of refraction
$\mathbf{P}$	Polarisation field
$\mathbf{P^{(1)}}$	Linear polarisation field
$\mathbf{P^{NL}}$	Nonlinear polarisation field
$\mathbf{P^{(n)}}$	n:th order nonlinear polarisation field
P	Polarisation field
$\mathbf{p}$	Momentum
R	Resonance enhancement factor

$\mathbf{r}$	3-dimensional point vector
S	Surface area
$\mathbf{v}$	Velocity
v	Speed
w	Arm width of the nanoparticle
x, y, z	Cartesian coordinates
χ	Electric susceptibility
$\chi^{(1)}$	Linear electric susceptibility
$\chi^{(n)}$	n:th order nonlinear electric susceptibility
$\chi^{(2)}_{ijk}$	2nd-order nonlinear electric susceptibility component ijk
ϵ	Relative permittivity
ϵ_0	Vacuum permittivity
ϵ'	Static permittivity
γ	Dipole damping rate
γ_D	Damping rate
Λ	Lattice constant
λ	Wavelength
λ_{ij}	Resonance mode wavelength
λ_{max}	Centre wavelength of resonance
μ_0	Vacuum permeability
ω	Angular frequency
ω_0	Resonance frequency
ω_j	Resonance frequency
ω_p	Plasma frequency
σ	Conductivity
θ	Waveplate rotation angle
ρ	Free charge density
ξ	Interaction strength parameter

FWHM	Full width at half maximum
HWHM	Half width at half maximum
HWP	Half-wave plate
LPF	Long-pass filter
NRT	Nonlinear response tensor
PMT	Photomultiplier tube
SH	Second-harmonic
SHG	Second-harmonic generation
SLR	Surface Lattice Resonance
SPF	Short-pass filter

1. INTRODUCTION

Optics, the study of light, is pervasive in the everyday life. Not only are most people very reliant on visual perception, but many technological advances in the recent decades rely on various optical phenomena. Examples of such advances include lasers with their numerous applications, ranging from DVD-players to industrial welding to space exploration, and modern telecommunications, which rely heavily on optical fibres. Many of these technologies and advances are all but necessary for the modern-day society, which highlights the importance of optics as an active field of research.

One of the many fields of optics is nonlinear optics, which studies optical effects for which the strength of the response is no more directly proportional to the strength of the input field. This means the observed effects scale nonlinearly, and allows for interesting phenomena such as self-modulation of the phase of the field or generation of new optical frequencies [1]. However, nonlinear effects are usually weak, and special materials and high intensities are often required to observe them. This means that nonlinear effects went largely undiscovered until the laser was invented in the 1960s.

In the past couple of decades, metal nanostructures have emerged as promising materials for both linear and nonlinear optics. Combining intrinsic electromagnetic properties of metals with nanoscale dimensions gives rise to particle plasmon resonances, which greatly shape the optical response of metal nanostructures [2]. Taking advantage of these plasmon resonances has allowed creation of optical metamaterials. Optical metamaterials are artificial materials with interesting optical properties, some of which have not been observed in nature. One example of these intriguing properties is negative index of refraction, which could be used to build so-called superlenses that are capable of bypassing the diffraction limit, thus allowing super-resolution imaging [3].

As a result of the interest in optical metamaterials and metal nanostructures, many different types of metal nanoparticles have been studied. Many studies have focused on the properties of particles of different shapes and sizes [4–15]. While the

properties of the individual particles have been found to be important, studies on interparticle effects indicate that both near-field and far-field coupling between the particles have significant effect on the optical properties of nanostructures [16–27].

The emphasis of this work is on the effect of the so-called surface lattice resonances (SLR) on both linear and nonlinear properties in arrays of gold nanoparticles. Modifying the resonance profile and wavelength via the interparticle coupling allows for new ways to tune the optical response of the structure, and thus understanding the effects of interparticle coupling is essential in designing and building functional metamaterials. It is also possible to take advantage of SLRs to make the response of a structure dependent on the angle of incidence [19, 21, 27].

In this work, L-shaped gold nanoparticles of three different sizes are studied. The particles are arranged in regular square arrays, some of which are designed to support SLRs near a plasmon resonance of the individual nanoparticles. Comparing the response of differently arranged nanostructures allows discerning the effect of the SLR from the individual particle resonance, and should provide valuable information about the effect of the SLRs.

This work was done in the Nonlinear Optics Group of the Laboratory of Photonics of Tampere University of Technology under the guidance of Dr. Robert Czaplicki and Prof. Martti Kauranen. Chapters 2 and 3 of this work present the background information required to understand the experimental results. Chapter 2 focuses on optical theory, while Chapter 3 covers relevant aspects of nanostructures. Chapter 4 contains the details on samples used, including the manufacturing process, and also describes the experimental setups that were used in the measurements. Chapter 5 presents the results and the respective discussions, and Chapter 6 concludes this Thesis and suggests possible future research prospects.

2. OPTICS

Optics is a branch of physics that studies the properties and behaviour of light. This Chapter covers parts of optical theory essential for understanding this work, including the fundamentals of wave motion, light as electromagnetic radiation, material response to light, and the basics of nonlinear optical phenomena.

2.1 Wave motion

A wave is a disturbance that travels in space, transferring energy without net transfer of matter. Examples of waves include water waves, sound waves, and vibrations in a string. A characteristic property of a wave is that, in a homogeneous and lossless medium, the disturbance travels at a constant velocity without changing its shape. Waves are classified depending on whether the disturbance is in a direction parallel or perpendicular to the direction of propagation of the wave; such waves are called longitudinal and transverse waves, respectively. Figure 2.1 shows the difference between these types of waves.

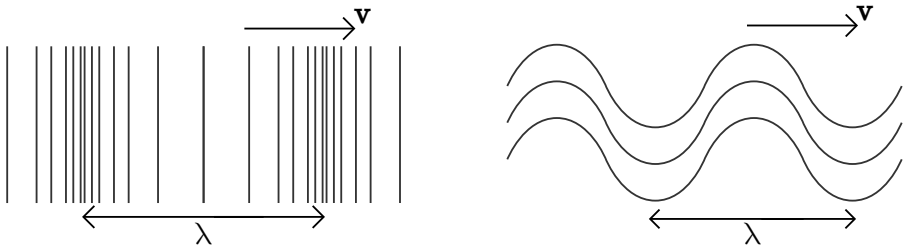

(a) Longitudinal wave **(b)** Transverse wave

Figure 2.1 *Longitudinal and transverse waves. The velocity of the wave is* $\mathbf{v}$ *and the wavelength of the wave is* λ*.*

Waves are often characterised by their wavelength λ and frequency f. These two quantites relate to each other via the equation

$$\lambda f = \frac{\omega}{k} = v, \tag{2.1}$$

where $k = 2\pi/\lambda$ is the wavenumber, $\omega = 2\pi f$ is the angular frequency, and v is the velocity of the wave. Waves also have amplitude, which indicates the maximum

value of the disturbance. In a homogenous, lossless medium, the disturbance $\mathbf{A}$ is a wave if it satisfies the classical wave equation

$$\nabla^2 \mathbf{A} = \frac{1}{v^2} \frac{\partial^2 \mathbf{A}}{\partial t^2}, \tag{2.2}$$

where v is the velocity of the wave. The wave equation is linear; that is, if there are two waves $\mathbf{A}_1$ and $\mathbf{A}_2$ that satisfy the wave equation 2.2, then their sum $\mathbf{A}_1 + \mathbf{A}_2$ also satisfies the wave equation and is also a wave. This phenomenon is called linear superposition of waves.

One example of a function satisfying the wave equation 2.2 is

$$\mathbf{A}(\mathbf{r}, t) = \mathbf{A}_0 e^{i\mathbf{k}\cdot\mathbf{r} - i\omega t} + c.c. \tag{2.3}$$

where $\mathbf{r}$ is point vector in space, $\mathbf{A}_0$ is the complex amplitude of the wave, $\mathbf{k}$ is the wave vector, i is the imaginary unit, and *c.c.* denotes the complex conjugate of the expression. The complex conjugate is required since physical waves are real-valued quantities. Waves of this form are monochromatic, which means they consist of a single frequency, and travel in the direction of the wave vector $\mathbf{k}$ which has modulus equal to the wavenumber $k = 2\pi/\lambda$. They are also often referred to as plane waves, because the wavefront forms an infinite plane perpendicular to the wave vector $\mathbf{k}$.

2.2 Maxwell's equations

Maxwell's equations are a set of four differential equations that describe the behaviour of electromagnetic fields. They are a fundamental part of classical electromagnetism and, as light is a form of electromagnetic radiation, a very important in the field of optics. Equations 2.4 – 2.7 are Maxwell's equations in matter, presented in the differential form:

$$\nabla \cdot \mathbf{D} = \rho \tag{2.4}$$

$$\nabla \cdot \mathbf{B} = 0 \tag{2.5}$$

$$\nabla \times \mathbf{E} = -\frac{\partial \mathbf{B}}{\partial t} \tag{2.6}$$

$$\nabla \times \mathbf{H} = \mathbf{J} + \frac{\partial \mathbf{D}}{\partial t}. \tag{2.7}$$

Here, $\mathbf{D}$ is electric displacement field, ρ free charge density, $\mathbf{B}$ magnetic flux density, $\mathbf{E}$ electric field, $\mathbf{H}$ magnetic field, and $\mathbf{J}$ free current density. Quantities $\mathbf{D}$, $\mathbf{E}$, $\mathbf{B}$

and $\mathbf{H}$ are related via equations

$$\mathbf{D} = \epsilon_0 \mathbf{E} + \mathbf{P} \tag{2.8}$$

$$\mathbf{H} = \frac{\mathbf{B}}{\mu_0} - \mathbf{M}, \tag{2.9}$$

where ϵ_0 is the vacuum permittivity, $\mathbf{P}$ polarisation density, μ_0 the vacuum permeability, and $\mathbf{M}$ magnetisation.

Maxwell's equations are named after the physicist and mathematician James Clerk Maxwell, who not only formulated early versions of the equations in the 1860s based on the work of Faraday, Ampère and Gauss, but also could derive a result suggesting the existence of electromagnetic waves [28]. Deriving this result for electromagnetic fields in vacuum using modern-day differential notation is relatively straightforward.

Let us assume a perfect vacuum, which means no free charges or currents and no material polarisation or magnetization, and therefore $\rho = 0$, $\mathbf{J} = 0$, $\mathbf{P} = 0$ and $\mathbf{M} = 0$. Then, let us calculate the curl of both sides of equation 2.6, starting with the left-hand side:

$$\nabla \times (\nabla \times \mathbf{E}) = \nabla(\nabla \cdot \mathbf{E}) - \nabla \cdot \nabla \mathbf{E} = -\nabla^2 \mathbf{E}, \tag{2.10}$$

where $\nabla \cdot \nabla = \nabla^2$ is the Laplace operator. The first step corresponds to identity

$$\nabla \times (\nabla \times \mathbf{F}) = \nabla(\nabla \cdot \mathbf{F}) - \nabla \cdot \nabla \mathbf{F}, \tag{2.11}$$

and last step stems from the fact that in the absence of free charges and polarisation,

$$\nabla \cdot \mathbf{D} = \epsilon_0 \left(\nabla \cdot \mathbf{E}\right) = 0, \tag{2.12}$$

meaning that the divergence of the electric field $\mathbf{E}$ vanishes.

Calculating the curl of the right-hand side of equation 2.6 yields

$$\begin{aligned} \nabla \times \left(-\frac{\partial \mathbf{B}}{\partial t}\right) &= -\frac{\partial \left(\nabla \times \mathbf{B}\right)}{\partial t} \\ &= -\mu_0 \frac{\partial \left(\nabla \times \mathbf{H}\right)}{\partial t} \\ &= -\mu_0 \frac{\partial}{\partial t} \frac{\partial \mathbf{D}}{\partial t} \\ &= -\mu_0 \epsilon_0 \frac{\partial^2 \mathbf{E}}{\partial t^2}. \end{aligned} \tag{2.13}$$

As a physical quantity, the magnetic flux density $\mathbf{B}$ can be assumed to be sufficiently

smooth in order to switch the order of curl and time derivative. Applying equations 2.7, 2.9 and 2.8 lets us represent the right side in terms of the electric field **E**.

Combining the left and the right sides (equations 2.10 and 2.13, respectively) leads to the equation

$$\nabla^2 \mathbf{E} = \mu_0 \epsilon_0 \frac{\partial^2 \mathbf{E}}{\partial t^2}, \tag{2.14}$$

which has the form of the classical wave equation 2.2. Similar treatment can be used to derive equivalent result for the magnetic flux density **B**. These results suggest the existence of a type of wave composed of electromagnetic fields, travelling at speed $c = 1/\sqrt{\mu_0 \epsilon_0}$.

Originally, Maxwell noted that the speed of the supposed electromagnetic wave was close to the experimentally determined values of the speed of light, and proposed that light could be a propagating electromagnetic disturbance [28]. Since then, the existence of electromagnetic waves has been proven, and light has been found to consist of such waves.

2.3 Light as electromagnetic radiation

Light, being electromagnetic radiation, consists of oscillating electric and magnetic fields that propagate in space. The electric and magnetic fields are perpendicular to each other, and are related to each other as described by Maxwell's equations (equations 2.4 – 2.7). The electric and magnetic fields are also perpendicular to the wave vector and the velocity of the wave, which means that light is a transverse wave [29].

Since many materials have weak interactions with magnetic fields, it is customary to represent light in terms of its electric field [29]. Thus, according to equation 2.3, a typical monochromatic plane wave is presented as

$$\tilde{\mathbf{E}}(\mathbf{r}, t) = \mathbf{A} e^{i\mathbf{k}\cdot\mathbf{r} - i\omega t} + c.c. \tag{2.15}$$

where **A** is the complex amplitude of the wave and the tilde denotes quantity that varies rapidly in time at the optical frequency ω. Again, the complex conjugate is required because electric fields are real-valued physical quantities. A field containing a range of discrete frequencies can be expressed as a sum

$$\tilde{\mathbf{E}}(\mathbf{r}, t) = \sum_n{}' \tilde{\mathbf{E}}_n(\mathbf{r}, t), \tag{2.16}$$

where the individual wave components are monochromatic plane waves, analogous

to equation 2.15, and the use of prime signifies that summation is done only over positive frequencies. Since many optical phenomena are frequency-dependent, it is often convenient to include the spatial dependence in the field amplitude. Thus, by defining the local amplitude

$$\mathbf{E}_n = \mathbf{A}_n e^{i\mathbf{k}_n \cdot \mathbf{r}}, \tag{2.17}$$

the field components can be written as

$$\tilde{\mathbf{E}}_n(\mathbf{r}, t) = \mathbf{E}_n e^{-i\omega_n t} + c.c. \tag{2.18}$$

and calculating the complex conjugate in equation 2.18

$$(\mathbf{E}_n e^{-i\omega_n t})^* = \mathbf{E}_n^* e^{i\omega_n t} \tag{2.19}$$

shows that it seems to be oscillating at frequency $-\omega_n$. Thus, defining $\mathbf{E}_n = \mathbf{E}(\omega_n)$ and noting that $\mathbf{E}^*(\omega_n) = \mathbf{E}(-\omega_n)$, condition which follows from requiring that fields are real-valued, the sum in equation 2.16 can be expressed as

$$\tilde{\mathbf{E}}(\mathbf{r}, t) = \sum_n \mathbf{E}(\omega_n) e^{-i\omega_n t}, \tag{2.20}$$

where summation is over both positive and negative frequencies.

The complex amplitude $\mathbf{E}(\omega_n)$ contains information about the polarisation state of the wave, which describes how the orientation and strength of the electric field changes in time. There are three defined states of polarisation: linear, circular, and elliptical polarisations.

At a fixed point in space, the electric field of linearly polarised light oscillates in a line as time progresses, whereas for circularly polarised light the electric field rotates around the propagation axis while its amplitude stays constant, effectively drawing a circle in the plane perpendicular to the propagation axis. In elliptically polarised light, the electric field also rotates, but its amplitude changes periodically during the rotation, thus drawing an ellipse.

Light can also exist in unpolarised and partially polarised states. Unpolarised light still has momentary polarisation, but that momentary polarisation is changing rapidly in a random fashion. The same is true for partially polarised light, except the random distribution of the momentary polarisation is weighted towards some mix of the defined polarisation states.

2.4 Wave-particle duality

As already established, light consists of electromagnetic waves, and thus exhibits wave-like qualities such as diffraction, refraction, reflection and superposition [29]. However, not all properties of light can be explained by treating it as a classical wave. Quantum mechanics provides the answer in wave-particle duality, which means that any wave will exhibit particle-like qualities, and vice versa [30].

This means that not only can light be understood as a propagating wave consisting of electromagnetic fields, but also as a stream of massless particles called photons. Such particles are the quanta of light, and the energy of each photon is [30]

$$E = hf = \frac{hc}{\lambda}, \tag{2.21}$$

where h is the Planck constant, f the frequency, λ the wavelength, and c the speed of light. Despite being massless, photons carry the momentum [29]

$$\mathbf{p} = \hbar\mathbf{k}, \tag{2.22}$$

where $\hbar = h/2\pi$ is the reduced Planck constant and $\mathbf{k}$ the wave vector, which points towards the movement direction of the wave and has magnitude $k = 2\pi/\lambda$.

The quantum mechanical treatment can explain, among other things, why transitions between the energy levels of materials (for example electronic transitions) only couple to specific, possibly very narrow wavelength bands. This is especially true in atomic matter, in which different energy levels are clearly defined and thus require photons of specific energy to excite [29].

2.5 Electric susceptibility

The material response to electric field is called polarisation[1]. In bulk matter, the important quantity is polarisation density $\mathbf{P}$ [29]. When polarisation density is non-vanishing, equation 2.14 is no more valid. However, it can be shown that for light in a dielectric material, with certain approximations, the wave equation becomes [1]

$$\nabla^2\tilde{\mathbf{E}} - \frac{1}{c^2}\frac{\partial^2\tilde{\mathbf{E}}}{\partial t^2} = \frac{1}{\epsilon_0 c^2}\frac{\partial^2\tilde{\mathbf{P}}}{\partial t^2}. \tag{2.23}$$

[1]Not to be confused with the polarisation of the electromagnetic wave, which is the orientation of its electric field $\mathbf{E}$.

Simple, yet often sufficient, treatment of the material response is to assume that the polarisation density due to the electric field of light is directly proportional to the applied electric field, which means that the polarisation can be written as [1]

$$\tilde{\mathbf{P}} = \epsilon_0 \chi \tilde{\mathbf{E}}, \tag{2.24}$$

where χ is the electric susceptibility of the (bulk) material. The materials in which equation 2.24 holds true are called linear materials. This means that equation 2.8 becomes

$$\mathbf{D} = \epsilon_0 \mathbf{E} + \epsilon_0 \chi \mathbf{E} = \epsilon_0 (1 + \chi) \mathbf{E} = \epsilon_0 \epsilon \mathbf{E}, \tag{2.25}$$

where $\epsilon = 1 + \chi$ is the relative permittivity of the material. The wave equation 2.23 can now be written

$$\nabla^2 \tilde{\mathbf{E}} - \frac{1 + \chi}{c^2} \frac{\partial^2 \tilde{\mathbf{E}}}{\partial t^2} = 0, \tag{2.26}$$

which means that the wave now travels at speed $v = c/\sqrt{1 + \chi}$. Thus, light travels at different speeds in different media. A quantity called refractive index, denoted n, is defined with the relation

$$v = \frac{c}{n}. \tag{2.27}$$

This leads to the relation $n = \sqrt{1 + \chi} = \sqrt{\epsilon}$, which holds true in typical non-magnetic bulk media.

Because susceptibility often depends on the frequency of the field, and calculating time-dependent polarisation can be complicated since it depends not only on the instantaneous field but also the past field, it is convenient to use Fourier transformed quantities in the frequency plane. This leads to the equation

$$\mathbf{P}(\omega) = \epsilon_0 \chi(\omega) \mathbf{E}(\omega), \tag{2.28}$$

where ω is the frequency of the electric field.

While the form of the equation 2.28 might suggest that polarisation field is parallel to the electric field, this is not necessarily true. To account for this, the electric susceptibility, in general, cannot be represented by a scalar number, and a three-by-three matrix must be used instead. This means that the electric susceptibility is a second-rank tensor (represented by three-by-three matrix), and has $3^2 = 9$ potentially independent components. The symmetry properties of the medium may require certain components to be vanishing, or dependent from each other.

For example, in completely isotropic materials, all optical properties of the material must be the same in all directions. This means that the tensor can be represented

by a scalar number and that polarisation density is aligned parallel to the electric field. In anisotropic materials, this is no longer true, and the optical properties such as refractive index and absorption will differ between the different components of the electric field polarisation. For example, many crystalline structures exhibit birefringence, where the index of refraction is different along different axes of the crystal [29].

2.6 Lorentz model of electric susceptibility

The Lorentz model is a relatively simple classical model of the material response to an external electric field [29,31]. It treats electron-nucleus pairs as damped harmonic oscillators driven by an external electric field. This kind of electron-nucleus pair forms an electric dipole, which has the electric dipole moment

$$\tilde{d} = -e\tilde{x}, \tag{2.29}$$

where e is the elementary charge and $\tilde{x}$ is the displacement of the electron from its equilibrium position. Assuming that the individual dipoles do not interact with each other, the material response is the sum of the responses of the individual dipoles.

Figure 2.2 depicts an oscillator made of such electron-nucleus pair. The force acting on the electron is assumed to be

$$\tilde{F} = m\frac{d^2\tilde{x}}{dt^2} = -e\tilde{E}(t) - 2m\gamma\frac{d\tilde{x}}{dt} - m\omega_0^2\tilde{x}, \tag{2.30}$$

where the first term is the force due to the electric field, the second is the damping force that is assumed to be proportional to the speed of the electron, and the third is the harmonic restoring force. In the equation, m is the mass of the electron, $\tilde{E}(t)$ is the external electric field, γ is the dipole damping rate, and ω_0 is the resonance frequency of the oscillator. To simplify the treatment, only one-dimensional scalar fields are considered.

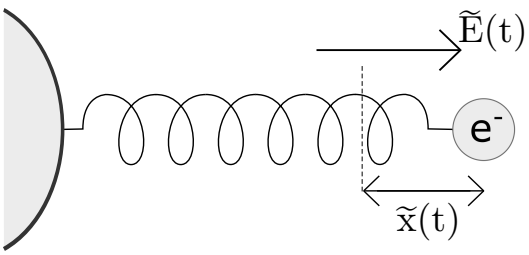

Figure 2.2 *In the Lorentz model, electrons in an electric field are treated as mechanical oscillators driven by an external force.*

Substituting the electric field[2]

$$\tilde{E}(t) = E_0 e^{-i\omega t}, \tag{2.31}$$

where E_0 is the field amplitude and ω the angular frequency, into equation 2.30 results in the second-order inhomogeneous differential equation

$$\frac{d^2\tilde{x}}{dt^2} + 2\gamma\frac{d\tilde{x}}{dt} + \omega_0^2\tilde{x} = -(e/m)E_0 e^{-i\omega t}. \tag{2.32}$$

It is reasonable to expect that the electron oscillates at a frequency equal to the frequency of the external field. Thus, the expected form of the solution is

$$\tilde{x}(t) = x_0 e^{-i\omega t}, \tag{2.33}$$

where x_0 is an arbitrary constant. The first and second derivatives of $\tilde{x}(t)$ are

$$\frac{d\tilde{x}(t)}{dt} = -i\omega x_0 e^{-i\omega t} \tag{2.34}$$

$$\frac{d^2\tilde{x}(t)}{dt^2} = -\omega^2 x_0 e^{-i\omega t}. \tag{2.35}$$

Substituting equations 2.33, 2.34, and 2.35 into equation 2.32 results in the equation

$$-\omega^2 x_0 e^{-i\omega t} - 2i\gamma\omega x_0 e^{-i\omega t} + \omega_0^2 x_0 e^{-i\omega t} = -(e/m)E_0 e^{-i\omega t}. \tag{2.36}$$

Solving 2.36 for x_0 yields

$$x_0 = \frac{-(e/m)E_0}{\omega_0^2 - \omega^2 - 2i\gamma\omega} \tag{2.37}$$

and thus the electron's displacement from equilibrium is

$$\tilde{x}(t) = -\frac{e}{m}\frac{E_0 e^{-i\omega t}}{\omega_0^2 - \omega^2 - 2i\gamma\omega} = -\frac{e}{m}\frac{\tilde{E}(t)}{D(\omega)} \tag{2.38}$$

where the denominator function D is defined as $D(\omega) = \omega_0^2 - \omega^2 - 2i\gamma\omega$.

Each oscillator has dipole moment $\tilde{d} = -e\tilde{x}$, and the total material polarisation under the electric field is sum of these (identical) dipole moments. Thus, the material polarisation density can be expressed as

$$\tilde{P}(t) = -eN\tilde{x}(t), \tag{2.39}$$

[2]The explicit complex conjugate of the field is omitted to simplify the equation, since solving the equation for the conjugate field is straightforward using the presented method.

where N is the number of electrons per unit volume. Combining equations 2.24, 2.38, and 2.39 and solving for susceptibility χ yields

$$\chi(\omega) = \frac{e^2}{m\epsilon_0}\frac{N}{D(\omega)}. \tag{2.40}$$

Equation 2.40 is valid as long as the electron density of the material is low enough so that the individual oscillators do not interact with each other. The susceptibility is a complex quantity. This means that since the susceptibility, permittivity, and refractive index are linked via relation

$$n(\omega) = \sqrt{\epsilon(\omega)} = \sqrt{1 + \chi(\omega)}, \tag{2.41}$$

the permittivity and refractive index are also complex quantities. The real part of the refractive index modifies the phase of a propagating wave, while imaginary part is related to absorption.

While the Lorentz model provides a decent approximation of the electric susceptibility, it has its weaknesses. For example, it fails to consider multiple energy levels of the material. This is fine as long as there is only a single resonance close to the frequency ω, but this is not always the case. If there are multiple resonances present, the total response is

$$\chi(\omega) = \frac{e^2}{m\epsilon_0}\sum_j \frac{N_j}{D_j(\omega)} \tag{2.42}$$

where summation is over all different resonances j, the denominator function is $D_j(\omega) = \omega_j^2 - \omega^2 - 2i\gamma_j\omega$, and N_j represents the oscillator strength of the resonance. Whenever $\omega^2 \approx \omega_j^2$, the imaginary part dominates, which leads to high absorption and material being non-transparent; otherwise, the susceptibility is mostly real and material is transparent.

2.7 Nonlinear optics

The common optical phenomena observed in everyday life are linear in their nature. This means that the strength of the phenomena is directly proportional to the incident light. However, with strong enough electromagnetic fields, the material response is no more linear, which results in some peculiar phenomena.

For the purposes of this work, only nonlinear phenomena arising from electric dipole interactions are considered. When a medium is exposed to a sufficiently strong electric field, nonlinear components appear in polarisation in addition to the linear

polarisation described by equation 2.24. This results in total polarisation

$$\tilde{\mathbf{P}} = \tilde{\mathbf{P}}^{(1)} + \tilde{\mathbf{P}}^{NL}, \tag{2.43}$$

where $\mathbf{P}^{(1)}$ is the linear and $\mathbf{P}^{NL}$ the nonlinear polarisation [1]. For many materials, the total polarisation can be expressed as power series

$$\tilde{\mathbf{P}} = \epsilon_0 \chi^{(1)} \tilde{\mathbf{E}} + \epsilon_0 \chi^{(2)} \tilde{\mathbf{E}}^2 + \epsilon_0 \chi^{(3)} \tilde{\mathbf{E}}^3 + ... \tag{2.44}$$

where $\chi^{(n)}$ is the n:th order electric susceptibility. Susceptibilities are tensor quantities and, in general, n:th order susceptibility is a tensor of rank $(n+1)$ [1]. The first term in equation 2.44 is the linear polarisation $\tilde{\mathbf{P}}^{(1)}$, while the rest form the nonlinear polarisation $\tilde{\mathbf{P}}^{NL}$. In this work, only the second-order nonlinear phenomena, arising from the second-order nonlinear susceptibility $\chi^{(2)}$, are considered.

It is common to represent the nonlinear polarisation components in the Fourier plane, where the second-order nonlinear polarisation is

$$\mathbf{P}^{(2)}(\omega) = \epsilon_0 \chi^{(2)}(\omega = \omega_n + \omega_m; \omega_n, \omega_m) \mathbf{E}(\omega_n) \mathbf{E}(\omega_m), \tag{2.45}$$

where the resulting polarisation field oscillates at the frequency $\omega = \omega_n + \omega_m$. The oscillating polarisation field acts as a source of a new wave. Therefore, the nonlinear polarisation can oscillate at different frequency than the incident fields, and thus create waves at new frequencies. One example of this phenomenon is sum-frequency generation, where a new wave at frequency $\omega = \omega_1 + \omega_2$ is created, with ω_1 and ω_2 being the frequencies of the incident waves [1].

Now, let us consider second-order nonlinear polarisation $\mathbf{P}^{(2)}(\mathbf{r}, t)$, at point $\mathbf{r}$ and time t, in a centrosymmetric material; that is, a medium that possesses a centre of inversion. The properties of a centrosymmetric material, including the second-order nonlinear susceptibility $\chi^{(2)}$, must be invariant under inversion operation $\mathbf{r} \to -\mathbf{r}$. The material polarisation and the external electric field are reversed under inversion $\mathbf{r} \to -\mathbf{r}$:

$$\mathbf{E}(\mathbf{r}, t) = -\mathbf{E}(-\mathbf{r}, t) \tag{2.46}$$

$$\mathbf{P}^{(2)}(\mathbf{r}, t) = -\mathbf{P}^{(2)}(-\mathbf{r}, t). \tag{2.47}$$

Now, the second-order nonlinear polarisation becomes

$$\begin{aligned}\mathbf{P}^{(2)}(\mathbf{r},t) &= -\mathbf{P}^{(2)}(-\mathbf{r},t)\\ &= -\epsilon_0\chi^{(2)}\mathbf{E}(-\mathbf{r},t)\mathbf{E}(-\mathbf{r},t)\\ &= -\epsilon_0\chi^{(2)}\left(-\mathbf{E}(\mathbf{r},t)\right)\left(-\mathbf{E}(\mathbf{r},t)\right)\\ &= -\epsilon_0\chi^{(2)}\mathbf{E}(\mathbf{r},t)\mathbf{E}(\mathbf{r},t)\\ &= -\mathbf{P}^{(2)}(\mathbf{r},t),\end{aligned} \tag{2.48}$$

which means that the only valid solution is $\mathbf{P}(\mathbf{r}) = 0$, since neither the vacuum permittivity nor the material susceptibility can change during inversion. This condition requires that $\chi^{(2)}$ vanishes in a centrosymmetric medium, thus forbidding second-order nonlinear effects. More generally, second-order nonlinearity is forbidden whenever the surrounding medium possesses inversion symmetry in the direction of the total electric field. However, local symmetry-breaking features, such as interfaces between different media, edges, or defects, may allow some second-order nonlinear response from an otherwise symmetry-forbidden medium [32, 33].

2.8 Second-harmonic generation

Let us now consider a case of sum-frequency generation where the incident waves have the same frequency ω, called the fundamental frequency. Now the nonlinear polarisation includes the component

$$\mathbf{P}(2\omega) = \epsilon_0\chi^{(2)}(2\omega;\omega,\omega)\mathbf{E}(\omega)\mathbf{E}(\omega) \tag{2.49}$$

which is oscillating at frequency 2ω. This means that the emitted wave oscillates at frequency 2ω and is called second-harmonic (SH). This process is called second-harmonic generation (SHG). SHG is a parametric process, which means it happens near-instantaneously and does not result in energy transfer between the electric fields and the medium. SHG can also be understood as a process in which two photons at frequency ω are annihilated and a new photon at frequency 2ω is created.

The individual components of the polarisation field depicted in equation 2.49 can be expressed as

$$P_i(2\omega) = \epsilon_0 \sum_{jk} \chi^{(2)}_{ijk}(2\omega;\omega,\omega)E_j(\omega)E_k(\omega), \tag{2.50}$$

where i, j, k refer to the Cartesian coordinates and the summation is done over all combinations of j and k. Considering that the emitted SH field is proportional and parallel to the polarisation field, this allows probing the susceptibility tensor

components of the material by analysing the polarisation of the emitted SH field in relation to the polarisation of the incident fields.

In SHG, the incident field is often from a single source, very commonly a laser. This means that the emitted SH field scales quadratically as a function of the incident field. Because of this, increasing the strength of the incident field leads to rapidly increasing nonlinear response. Thus, increasing the strength (and power) of the fundamental field allows for easier observation of the nonlinear response. This makes lasers the light source of choice for studying nonlinear phenomena. To reach strong (instantaneous) fields, lasers operating in pulsed mode are often used, and the (local) field strength can be increased by focusing the beam.

2.9 Nonlinear Lorentz model

It is possible to expand the Lorentz model introduced in Chapter 2.6 to include higher-order susceptibilities [1]. The harmonic oscillator model that was used to model linear susceptibility is symmetric, which means that no second-order nonlinearity can arise from it. Thus, an asymmetric, anharmonic oscillator has to be considered. Like in Chapter 2.6, the treatment is restricted to one-dimensional scalar fields. Expanding the restoring force into

$$\tilde{F}_{restoring} = -m\omega_0^2\tilde{x} - ma\tilde{x}^2, \tag{2.51}$$

where a is a parameter describing the strength of the nonlinearity, satisfies the requirement of asymmetry. The equation of motion of the electron becomes

$$\frac{d^2\tilde{x}}{dt^2} + 2\gamma\frac{d\tilde{x}}{dt} + \omega_0^2\tilde{x} + a\tilde{x}^2 = -(e/m)E_0e^{-i\omega t} \tag{2.52}$$

when the external field is oscillating at frequency ω.[3] While there are no known general solutions to equation 2.52, a good approximate solution can be achieved if the field is sufficiently weak so that for any induced displacement $\tilde{x}$, the nonlinear term $a\tilde{x}^2$ is much smaller than the linear term $\omega_0\tilde{x}$. As long as this holds, a solution can be found using perturbation expansion [1], where the electric field is replaced by $\xi E_0e^{-i\omega t}$, and ξ is a dimensionless parameter with value between zero and one. The solution is assumed to have form

$$\tilde{x} = \xi\tilde{x}^{(1)} + \xi^2\tilde{x}^{(2)} + \xi^3\tilde{x}^{(3)} + ... \tag{2.53}$$

[3] In general, second-order nonlinearities allow two fields of different frequencies to interact, as can be seen from equation 2.45. However, for the purposes of this work, the treatment focuses on SHG process in the case of a single incident field oscillating at frequency ω.

and the terms proportional to any arbitrary power of ξ are required to satisfy equation 2.52 separately. To achieve a model for second-order nonlinearity, terms proportional to ξ and ξ^2 need to be considered. This leads to the equations

$$\frac{d^2\tilde{x}^{(1)}}{dt^2} + 2\gamma\frac{d\tilde{x}^{(1)}}{dt} + \omega_0^2\tilde{x}^{(1)} = -(e/m)E_0e^{-i\omega t} \tag{2.54}$$

$$\frac{d^2\tilde{x}^{(2)}}{dt^2} + 2\gamma\frac{d\tilde{x}^{(2)}}{dt} + \omega_0^2\tilde{x}^{(2)} + a\left[\tilde{x}^{(1)}\right]^2 = 0. \tag{2.55}$$

Equation 2.54 is the same as equation 2.32, and its solution was found to be

$$\tilde{x}^{(1)}(t) = -\frac{e}{m}\frac{E_0e^{-i\omega t}}{D(\omega)}. \tag{2.56}$$

Complex conjugates are implicitly assumed to be included in both the external electric field and the displacement $\tilde{x}^{(1)}$. This means that the square of $\tilde{x}^{(1)}$ includes terms at frequencies 0 and $\pm 2\omega$. Equation 2.55 can be solved for each frequency separately, and therefore the solution for frequency 2ω can be obtained by solving the equation

$$\frac{d^2\tilde{x}^{(2)}}{dt^2} + 2\gamma\frac{d\tilde{x}^{(2)}}{dt} + \omega_0^2\tilde{x}^{(2)} = -a\left(\frac{eE_0}{m}\right)^2\frac{e^{-2i\omega t}}{D^2(\omega)} \tag{2.57}$$

using the treatment presented in Chapter 2.6. The solution to equation 2.57 is found to be

$$\tilde{x}^{(2)}(t) = -a\left(\frac{eE_0}{m}\right)^2\frac{e^{-2i\omega t}}{D(2\omega)D^2(\omega)}. \tag{2.58}$$

Noting that the second-order nonlinear polarisation for SHG is

$$P^{(2)}(2\omega) = \epsilon_0\chi^{(2)}E^2(\omega) \tag{2.59}$$

and that the polarisation can be expressed in terms of the sum of the individual dipole moments (equation 2.39), the second-order susceptibility is found to be

$$\chi^{(2)} = \frac{ae^3}{\epsilon_0m^2}\frac{N}{D(2\omega)D^2(\omega)} \tag{2.60}$$

when the number density N is small enough so that the individual oscillators do not interact with each other.

3. METAL NANOSTRUCTURES

This Chapter presents the electromagnetic and optical properties of metals and discusses the nature and properties of plasmon resonances. The optical properties of metal nanostructures are also discussed, and special focus is given to L-shaped nanoparticles that are the emphasis of this work.

3.1 Electromagnetic properties of metals

Metals have greatly different optical properties compared to dielectrics. The differences largely arise from the higher electric conductivity σ of metals. Chapter 2.5 discussed the electric susceptibility in dielectric materials. In dielectric materials, there are no free charge carriers available, and thus the conductivity is very close to zero and the free charge and current densities are negligible. In contrast, there is a large number of free charge carriers in metals, which greatly affects their response to electric and magnetic fields. In a medium where the assumption $\mathbf{J} = 0$ is no more valid, the wave equation becomes

$$\nabla^2\tilde{\mathbf{E}} - \frac{\epsilon}{c^2}\frac{\partial^2\tilde{\mathbf{E}}}{\partial t^2} = \frac{1}{\epsilon_0 c^2}\frac{\partial \mathbf{J}}{\partial t}. \tag{3.1}$$

In a conductive medium with the conductivity σ, the current density is

$$\mathbf{J} = \sigma\mathbf{E}, \tag{3.2}$$

and the (complex) relative permittivity becomes [2]

$$\epsilon'(\omega) = \epsilon(\omega) + i\frac{\sigma(\omega)}{\epsilon_0\omega}, \tag{3.3}$$

where ϵ is the static permittivity, which is linked to the polarisation of the medium under an external electric field. The refractive index of a conducting medium is thus

$$n(\omega) = \sqrt{\epsilon'(\omega)} \tag{3.4}$$

and, as it is complex-valued, means that conductive materials absorb light.

The response of metals to an external electric field can be described using a plasma model, in which a cloud of free electrons moves against a background of positive ions. From the classical equations of motion for these electrons, it is possible to derive the Drude model for the electric permittivity in metals [2]

$$\epsilon(\omega) = 1 - \frac{\omega_p^2}{\omega^2 + i\gamma_D\omega} = 1 - \frac{\omega_p^2}{\omega^2 + \gamma_D^2} + i\frac{\omega_P\gamma_D}{\omega\left(\omega^2 + \gamma_D^2\right)}, \tag{3.5}$$

where ω_P is the plasma frequency of the metal, ω is the angular frequency of the external field, and γ_D is the damping rate. The plasma frequency is the natural oscillation frequency of the electron sea, whereas the damping results from collisions between the electrons and the lattice ions.

For gold, which is the metal used in the samples studied in this work, the plasma frequency and damping rate are much larger and smaller, respectively, than optical frequencies. From the Drude model it can be seen that at optical frequencies, the real part of the electric permittivity of gold is negative, which is required for the existence of so-called plasmon resonances [2].

The Drude model provides a good estimate as long as the frequency of the electric field is not near the interband transitions of metal. However, for some metals, there are interband transitions occurring at optical frequencies, and for such metals the simple Drude model presented in equation 3.5 is no more valid. In this case, it is possible to expand the Drude model with the Lorentz model presented in chapter 2.6 to account for the presence of these transitions [2].

3.2 Plasmons

When the plasma frequency of a metal is significantly high compared to optical frequencies, the real part of the permittivity of the metal is negative and light-induced resonant collective oscillations of the conduction electrons can occur. Modes of these resonant oscillations are called plasmons [2]. Three kinds of plasmons exist, differentiated by how they are confined. Figure 3.1 presents the three different types of plasmons. The confinement of a plasmon mode greatly affects how it couples to optical fields.

Volume plasmons are longitudinal oscillations of the conduction electrons (Figure 3.1a). They appear in bulk metals and are not spatially confined. Because of their longitudinal nature, volume plasmons cannot be excited by transverse electromagnetic waves such as light.

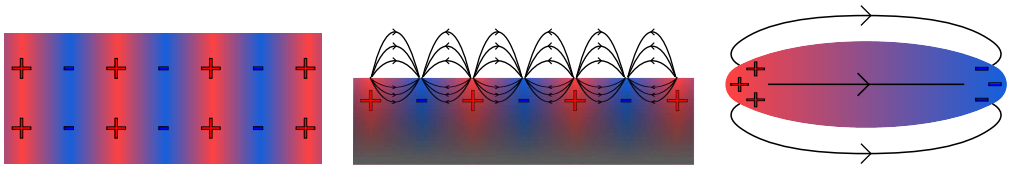

(a) Volume plasmons **(b)** Surface plasmons **(c)** Particle plasmons

Figure 3.1 *Different types of plasmons.*

Surface plasmons are oscillations confined in one dimension to the interface of a dielectric and a metal (Figure 3.1b) and, unlike volume plasmons, can be excited with electromagnetic waves. Surface plasmons can be observed when an electromagnetic wave travels along the interface and the electric field of the wave penetrates into the metal. This results in oscillations of the conduction electrons near the metal surface. Exciting surface plasmons over long travel distance requires specialised structuring of the interface to match the velocities of the wave in the metal and the dielectric, or the interaction will rapidly decay over distance as the phase difference between waves on different sides of the interface grows.

The third type of plasmons, called particle plasmons or localised surface plasmons, are confined in all three spatial dimensions (Figure 3.1c). They are observed, for example, in metal nanoparticles that have dimensions comparable to, or smaller than, the wavelength of light [2]. This makes them the most interesting type of plasmon resonances in the context of this work.

3.3 Metal nanoparticles

As established in the previous chapter, metal nanostructures with features below micrometer scale exhibit plasmon resonances excitable by visible and infrared light. These resonances shape the optical response of metal nanostructures, and modifying the resonances of the structures allows tailoring the optical response to a great degree or achieving optical properties not present in traditional materials. This has led to the creation of optical metamaterials with optical properties not found in nature, such as negative refractive index [34], which allows, for example, construction of superlenses capable of focusing light beyond the diffraction limit [3].

The intriguing possibilities offered by metamaterials has generated great interest in the study of metal nanoparticles, and many different kinds of metal nanoparticles have been studied over the past decades. Some examples include bars [7,15], triangles [5,8,9], nanorings [4,14], split-ring resonators [10–12], and L-shaped particles [6,13, 15]. Differently shaped and sized particles differ greatly in how different wavelengths

and polarisations couple to the plasmon resonances [35]. Possible near-field coupling between closely separated particles also play a role in the resonances [17].

An interesting aspect of metal nanoparticles is their characteristic property of enhancing local electromagnetic fields within or near the structures. This allows, for example, enhancing signal levels from inherently weak optical processes, like in surface-enhanced Raman spectroscopy [2, 36]. The local-field enhancement can result from the coupling between the incident electromagnetic field and the plasmon resonances, or from the lightning-rod effect. In lightning-rod effect, small features such as gaps or sharp tips cause localisation of electric charge in small volumes, which leads to large potential differences. It is important to note that the strength of the former effect depends on the wavelength of the incident field, but the strength of the lightning rod effect does not [37].

3.4 Nonlinear optical properties

Many types of metal nanoparticles have relatively strong nonlinear optical responses, which are typically enhanced when the fundamental frequency is near the plasmon resonance of the particles [2]. Other contributing factors particle geometry [38] and interactions between individual particles [2, 24, 27].

These factors combined with the small scale of the particles make it challenging to describe the nonlinear response of nanoparticles in full detail. Not only is the nonlinear susceptibility a locally varying quantity, but also the local electromagnetic field can vary a lot due to the local field enhancement. Also, for a detailed approach, coupling between the local, incoming, and generated fields would have to be accounted for. Because of all these contributing factors, describing the nonlinear response of the particles on the nanoscale is complicated.

However, for experimental studies, many of these problems can be avoided by defining a nonlinear response tensor (NRT) which connects the incident and emitted macroscopic fields [39]. Using this notation, the SH field emitted by a sample is

$$E_i(2\omega) = \sum_{jk} A_{ijk} E_j(\omega) E_k(\omega), \tag{3.6}$$

where the sum is over all possible combinations of j and k. The NRT A is a macroscopic quantity, and thus avoids difficulties related to nanoscale effects by treating the experiment as a "black box". It is, however, specific to the used experimental configuration, which limits the amount of information that can be obtained. Despite this, it is still an useful tool in studying the macroscopic response of nanoparticles.

3.5 Resonance enhancement

Near the resonance, nanoparticles typically exhibit strong local-field enhancement, increase in the scattering and absorption coefficients, and also stronger nonlinear response [2,40]. The resonance enhancement for the second-order nonlinear response can be modeled using the Lorentz model, introduced in Chapters 2.6 and 2.9, which results in the relation

$$\chi^{(2)} \propto \frac{N}{D(2\omega)D^2(\omega)} \tag{3.7}$$

where the denominator function is $D(\omega) = \omega_0^2 - \omega^2 - 2i\gamma\omega$. The damping factor γ is equal to the half width at half maximum (HWHM) of the resonance.

From the form of equation 3.7, it is expected that the closer the fundamental frequency is to the resonance, the more SHG is enhanced. Additionally, narrower resonance should lead to increased resonance enhancement, and the effect of the number density N should be linear, with higher number density of particles leading to stronger response.

3.6 Surface lattice resonances

Surface lattice resonances (SLR) arise from so-called diffractive coupling between the particles in a lattice. Diffractive coupling is a far-field interaction between fields scattered from individual particles [16]. Scattering occurs in all directions, but when scattered waves propagate within the lattice, their phases relative to each other lead to constructive or destructive interference at the locations of the particles, not unlike in diffraction from a grating. The relative phases are dependent on the optical path length between particles [19, 20].

If the optical path length between adjacent particles in the lattice is such that the scattered fields from the particles have a relative phase difference of 2π (or multiples thereof), the fields experience constructive interference. In a two-dimensional square lattice, the SLR mode wavenumber follows the relation [21, 41]

$$k_{ij} = n\frac{2\pi}{\lambda_{ij}} = \frac{2\pi}{\Lambda}\sqrt{i^2 + j^2}, \tag{3.8}$$

where n is the refractive index of the medium surrounding the lattice, λ_{ij} is the resonance wavelength of the mode, Λ is the lattice constant, and i and j are integers corresponding to different modes of the resonance. It is important to note that if the lattice is surrounded by different media from different sides, the modes in the two media are different and all of them can affect the response of the structure.

When the SLR mode is near the plasmon resonance mode of the individual particles, the total resonance of the complete nanostructure is shaped by both of them. As plasmon and surface lattice resonances are effectively continuous and discrete resonances, respectively, this results in so-called Fano resonances with characteristic asymmetric lineshapes [42]. It is possible, for example, to use this interaction to achieve higher-quality resonances to increase the resonance enhancement of the structure [22, 24, 25, 27].

In addition to the factors discussed above, the angle of incidence affects which wavelengths couple to the SLR modes. Increasing the angle of incidence has been found to red-shift the surface lattice resonance modes [21, 24, 27]. This allows fine-tuning the resonance to the desired wavelength by varying the angle of incidence.

3.7 L-shaped nanoparticles

In this work, L-shaped particles of different sizes and orientations are studied. L-shaped nanoparticles are called such after their shape, which resembles an uppercase L. Rotating the L-shape by 45° results in a configuration sometimes called the V-particle. This kind of V-particle is depicted in Figure 3.2a. L-shaped nanoparticles are characterised by the length and the width of the arms, both of which affect the optical response of the particles [43].

Ideal L-nanoparticles have plane of inversion between the two arms. The coordinate system for L-particles is set so that one axis (here, y) runs along the plane of symmetry, and the other (x) perpendicular to it. Due to the inherent symmetry of the particle, certain second-order nonlinear susceptibility tensor components vanish. It has been shown that only the components with even number of x are allowed in particles possessing this kind of symmetry [39].

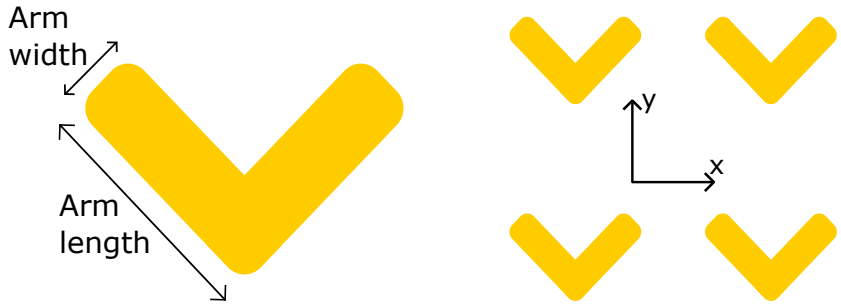

(a) L-shaped nanoparticle **(b)** Sample geometry

Figure 3.2 *a) L-shaped nanoparticle in* V*-configuration, and b) an example of sample geometry and the used coordinate system.*

Since L-nanoparticles are anisotropic, their linear (and nonlinear) optical properties depend on the polarisation of the incident field. It is typical for the L-particles to be mostly transparent, but exhibit high extinction over a narrow wavelength range. This peak results from coupling between the incident field and the plasmon resonance of the particles [13, 15]. The resonance wavelength depends on the dimensions of the particles and is typically different for x- and y-polarised light. This dichroism arises from the fact that in y-polarised resonance, the oscillations happen along the lengths of the arms, but in x-polarised resonance the oscillation is over the whole length of the L-shape. Therefore, it is expected that the x-polarised resonance occurs at higher wavelength than the y-polarised resonance [43].

To study the effects of coupling between L-nanoparticles, samples with the nanoparticles in regular lattices are manufactured. Figure 3.2b depicts one possible sample geometry with the coordinate system used in this work. In such a sample, the lattice constant is defined as the size of the unit cell (which contains exactly one particle). Modifying the lattice constant to allow different lattice resonance modes can be used to tune the optical properties of the sample [32].

As previously discussed, nonlinear optical properties of L-nanoparticles depend on the polarisation of the incident fields, with some tensor components being symmetry-forbidden for SHG. Additionally, as there are multiple parameters that affect the nonlinear response, it is convenient to use the macroscopic nonlinear response tensor formalism presented in Chapter 3.4. Thus, the SH response of an ideal sample at normal incidence is

$$E_i(2\omega) = A_{ixx}E_x^2(\omega) + A_{iyy}E_x^2(\omega) + 2A_{ixy}E_x(\omega)E_y(\omega), \tag{3.9}$$

where i is either x or y. The factor of two results from the fact that for SHG $A_{ixy} = A_{iyx}$. As some nonlinear tensor components vanish due to symmetry, the components of the generated SH field are

$$E_x(2\omega) = 2A_{xxy}E_x(\omega)E_y(\omega) \tag{3.10}$$

$$E_y(2\omega) = A_{yxx}E_x^2(\omega) + A_{yyy}E_y^2(\omega). \tag{3.11}$$

However, this is only valid for a perfect sample. Imperfections in the nanoparticles can break the symmetry and cause supposedly forbidden tensor components be non-vanishing [33, 44].

4. EXPERIMENTAL METHODS

In this Chapter, the fabrication process of the samples is described, and the principles behind the design of the samples is also discussed. The experimental setups used in both linear and nonlinear measurements are also presented.

4.1 Sample fabrication

The samples studied in this work were fabricated by Dr. Ismo Vartiainen at the University of Eastern Finland using electron-beam lithography. The material used for the nanoparticles was gold, and the used substrate was 0.5 mm thick fused silica plate. The steps of the fabrication process are shown in Figure 4.1. In electron-beam lithography, the substrate is first coated with resist sensitive to the energy of the electron-beam. A thin copper layer is deposited on top of the resist layer. The purpose of this copper layer is to prevent accumulation of electric charge during the electron-beam exposure. The next step is to write the desired structure on the resist with the electron-beam, after which the sample is developed. The type of resist used dictates the writing process; for some resists the areas exposed to the electron-beam are removed in the development, while for others the exposed areas remain and the areas that were not exposed are removed. After the development, a

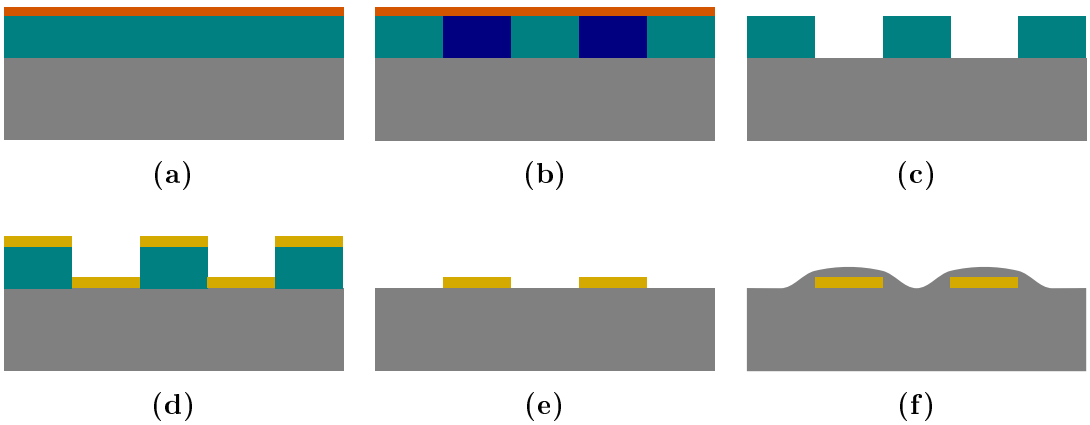

Figure 4.1 *Sample fabrication process. a) Deposition of the resist and copper layers. b) Writing with electron-beam. c) Development. d) Deposition of the adhesion and gold layers. e) Removal of the remaining resist. f) Deposition of the protective quartz layer.*

thin layer of chromium is deposited on the sample to act as an adhesion layer for the gold layer that forms the actual nanostructures. Once the gold layer is deposited, the remaining resist and the metal on top of it are removed in a solvent bath. This leaves only the desired nanostructure on the substrate. In the final step, a layer of evaporated quartz is deposited on top of the structures for protection.

4.2 Samples

The samples studied in this work consist of arrays of L-shaped gold nanoparticles of different arm lengths. The arm width of the nanoparticles was 100 nm and the nanoparticle thickness was 20 nm for all samples. In this work, "pitch" of the array is the centre-to-centre distance between adjacent nanoparticles in x- and y-directions, and "lattice constant" refers to the size of the unit cell in the array, which does not necessarily coincide with the pitch.

The arm lengths of the nanoparticles were chosen so that the nanoparticles have a strong plasmon resonance mode near the laser wavelength (1060 nm). Then, in order to study the effect of the SLRs, pitches were tuned so that some samples support a SLR mode near the laser wavelength.

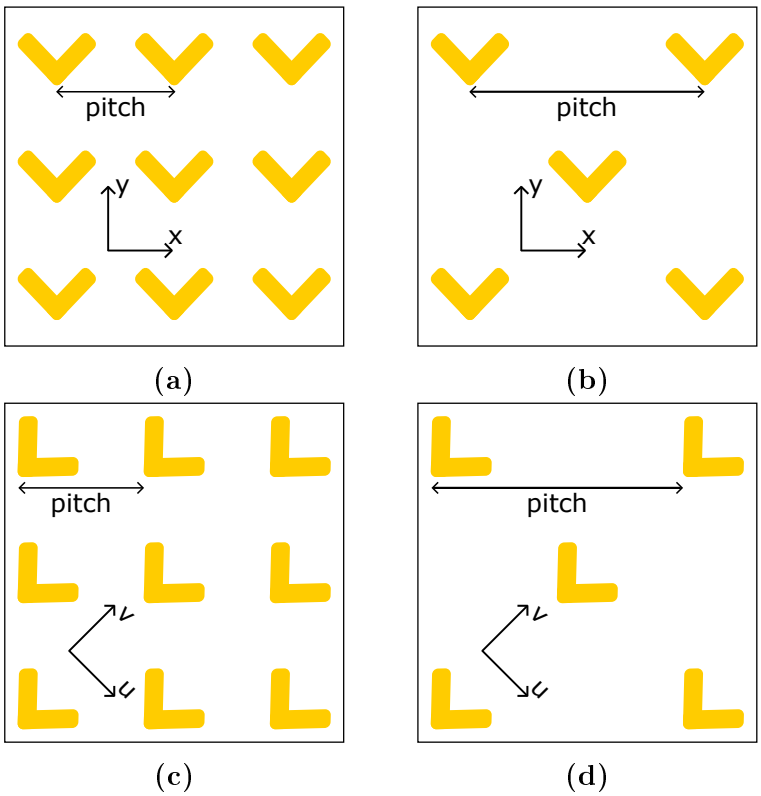

Figure 4.2 *Array configurations and coordinate systems for Samples a) 1a–1c and 3a–3b, b) 1d and 3c–3d, c) 2a–2c, and d) 2d.*

Table 4.1 *Lattice constants Λ and first- and second-order SLR modes λ_{10} and λ_{11}, respectively, for different samples.*

Samples	Λ(nm)	λ_{10}(nm)	λ_{11}(nm)
1a, 2a, 3a	500	725	513
1b, 1d, 2b, 2d, 3c	707	1025	725
3d	731	1060	750
1c, 2c, 3b	1000	1450	1025

Sample sets 1 and 2 have pitches 500 nm, 707 nm, 1000 nm, and 1000nm for Samples a, b, c, and d, respectively. In Samples a–c, all points of the array contain a particle, whereas Samples d are similar to Samples a except every other point of the array is empty. The empty array point is alternated between rows like shown in Figures 4.2b and 4.2d. This results in a square lattice that is rotated by 45° compared to Samples a–c, and has a lattice constant of 707 nm. In sample set 1, the nanoparticles have arm length of 275 nm and are in V-configuration. In set 2, the arm length is 250 nm and particles are in L-configuration, and the particle coordinate system (u, v) is rotated by 45° compared to the lattice coordinates (x, y). Figure 4.2 presents the different arrays and coordinate systems used for the samples.

Samples 3a–3c contain arrays of nanoparticles with arm length of 175 nm, and 3d with 180 nm arm length. The pitches of Samples 3a–d are 500 nm, 707 nm, 1000 nm, and 1034 nm, respectively. Samples 3a and 3b have arrays with all points filled (Figure 4.2a), whereas for 3c and 3d every other lattice point is empty. Thus, Samples 3c and 3d have rotated square lattices (Figure 4.2b) with lattice constants of 707 nm and 731 nm, respectively.

Lattice constants Λ and the wavelengths of the first- and second-order SLR modes λ_{10} and λ_{11}, respectively, for different samples are presented in Table 4.1. The refractive index of the used substrate is 1.45. As can be seen from the wavelengths of the modes, most samples support either first- or second-order SLR mode near the laser wavelength, with the exception of Samples 1a, 2a and 3a with lattice constant (and pitch) of 500 nm.

4.3 Linear measurements

The extinction spectra of the samples were measured using a microscope-like spectrometer setup presented in Figure 4.3. The setup measures total extinction, which includes both absorption and scattering. While these quantities cannot be determined individually, it should not be a problem as both contribute to the resonances.

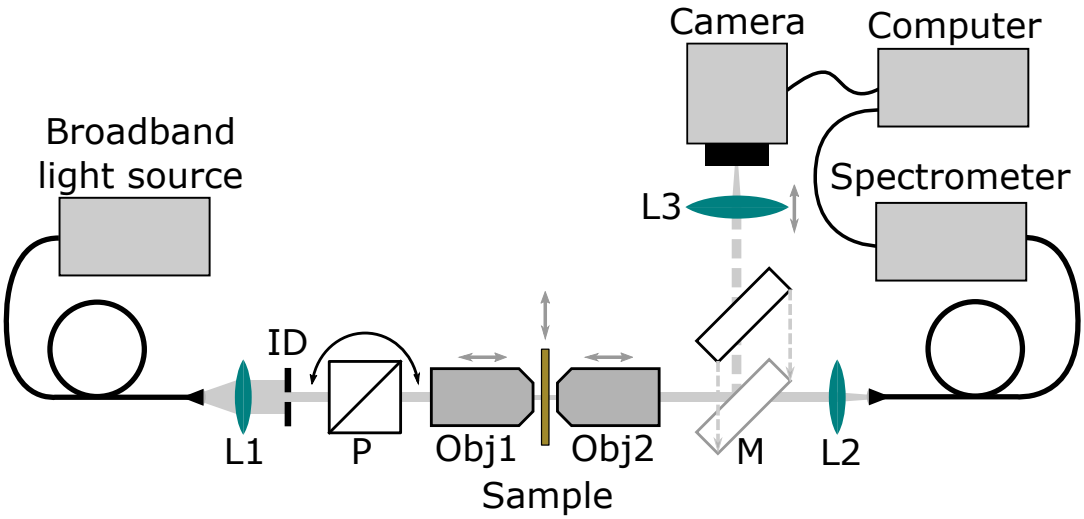

Figure 4.3 *Experimental setup used for measuring extinction spectra.*

In the extinction setup, a fibre-coupled broadband light source (Thorlabs SL201) was used to provide illumination on the sample. Light exiting the fibre spreads into a cone, which was collimated using positive lens L1. After lens L1 the collimated light passes through iris diaphragm ID, which was used to control the power incident at the sample. The iris diaphragm was adjusted so that without sample, the spectrometer was almost at saturation. This ensured best possible signal-to-noise ratio. After the iris, light passes through linear polariser P, which was required to study the polarisation-dependence of the resonances. Linear polarisations along x- and y-axes were used for samples 1a-d and 3a-3d, and linear polarisations along u- and v-axes for samples 2a-d. The polarised light was then focused on the sample using objective 1, and then re-collimated with objective 2. Both objectives were on linear translation mounts in order to accurately focus the light onto the sample. The sample was on a two-dimensional translation mount to allow moving between different sample areas. The collimated light coming out of objective 2 was then coupled into a fibre using lens L2. This fibre was connected to a spectrometer. In order to cover broad enough spectrum, measurements were repeated with two different spectrometers: Avantes AvaSpec-2048 and Avantes NIR256 with 400-1000 nm and 900-1700 nm spectral ranges, respectively.

The camera was used to aid in setting up the measurements. A movable mirror M was used to divert the light into the secondary arm of the setup, where lens L3 was used to focus the light onto the camera. The position of lens L3 was adjustable to facilitate focusing the camera on the sample in order to attain a sharp picture.

4.4 Nonlinear measurements

The experimental setup presented in Figure 4.4 was used to measure SHG from the samples. The source of the fundamental field is a mode-locked Nd:glass laser (Time-Bandwidth Products GLX-200, continuous power approximately 200 mW) operating in pulsed mode (pulse length 200 fs, repetition rate 82 MHz) at the wavelength of 1060 nm. The beam from the laser first passes through Faraday isolator FI to prevent any reflections from the setup entering the laser, and the power of the subsequently linearly polarised beam is then lowered to the desired level (in this work, 8 mW at the sample) using half-wave plate HWP1 and linear polariser P1. Half-wave plate HWP2 was used to align the incident linear polarization so that it was p-polariser (in the plane of reflection), which was orthogonal to the y-axis of the sample coordinate system.

In order to generate arbitrary linear polarisation from the linearly polarised incident beam, half-wave plate HWP3 was used. HWP3 was installed on a rotating mount actuated by an electric motor. This allowed controlling the polarisation of the beam during the measurements to a very high precision. The electric field components after the wave plate HWP3 are

$$E_x(\omega) = E_0(\omega)\cos(2\theta) \tag{4.1}$$

$$E_y(\omega) = E_0(\omega)\sin(2\theta), \tag{4.2}$$

where θ is the angle between the fast axis of the HWP3 and the x-axis of the sample coordinate system. Rotating the wave plate allowed measuring SHG from the sample with different fundamental field polarisations. Because the wave plates (or other components) may have weak SHG response, long-pass filter LPF was used to block

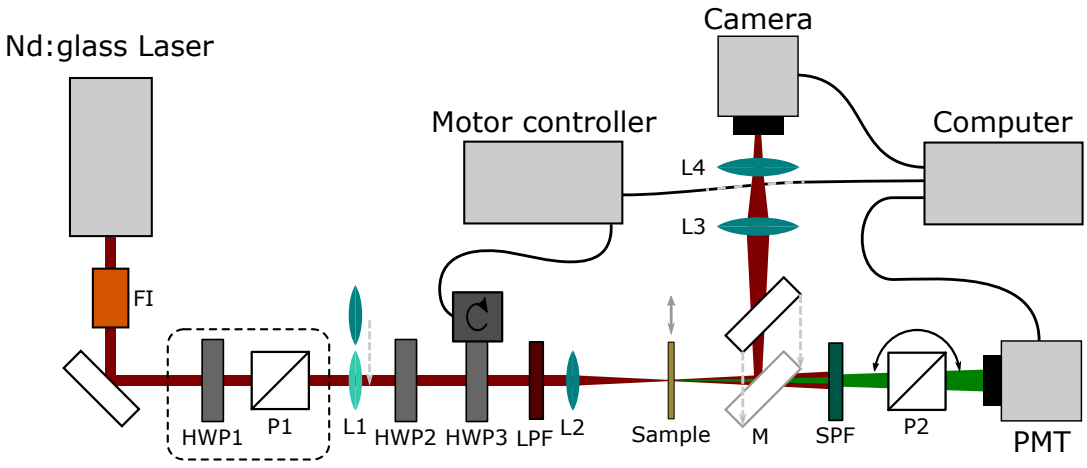

Figure 4.4 *Experimental setup used for measuring SHG.*

SH signals from interfering with the measurements. The beam was then focused onto the sample using lens L2. The focal length of lens L2 was chosen to be relatively long to keep the beam as close to a plane wave as possible. After the sample, the fundamental wavelength was removed from the beam using short-pass filter SPF. Linear polariser P2 was used as analyser, set to pass y-polarised light for samples 1a-d and 3a-d, and v-polarised light for samples 2a-d. Finally, a photomultiplier tube PMT (Becker & Hickl GmbH PMC-100-0) connected to a photon-counting card (Becker & Hickl GmbH PMS-400A) was used as detector system. A computer running a specific measurement program was used to control the angle of HWP3 and record the intensity measured by the photomultiplier tube. Because of the high sensitivity of the detector system, the setup was enclosed inside a box in a carefully darkened room in order to reduce the background noise levels to as low as possible.

Like in the setup used for measuring the extinction spectra, the camera was used to align the sample. The sample was mounted on a three-dimensional translation mount, allowing both moving between sample areas and precisely setting the sample in the focus of lens L2 to achieve maximum signal-to-noise ratio. Removable mirror M was used to divert the beam into the secondary arm of the setup and lenses L3 and L4 were used to focus the beam onto the camera. Removable lens L1 was used to enlarge the beam at sample when the camera was in the use. Lens L1 was necessary because of the focusing lens L2, as without L1 only the small focus of lens L2 would have been seen on the camera.

5. RESULTS AND DISCUSSION

This Chapter presents the results of both extinction and SHG measurements. Quantitative and qualitative analysis of the results is also included in this Chapter.

5.1 Extinction spectra

The extinction spectrum of each sample was measured for two polarisations: x and y for V-configuration Samples 1a–d and 3a–d, and u and v for L-configuration Samples 2a–d. The results are presented in Figures 5.1a – 5.1f. As expected, the extinction peaks for y- or v-polarised light occur at a shorter wavelength than for x- or u-polarised light [43, 45]. The sample parameters and results for different samples are detailed in Table 5.1.

The nanoparticle dimensions were chosen so that each type of particle would have at least one of its resonances near the laser wavelength (1060 nm). For Samples 2a–d with arm length of 250 nm, such resonance was observed with v-polarised light, and for Samples 1a–d with arm length of 275 nm, a resonance near laser wavelength was observed with y-polarised light. The resonances in Samples 1a–d were red-shifted

Table 5.1 *Sample parameters, including arm lengths of the particles and lattice constants* Λ*, and resonant polarisations, centre wavelengths* λ_{max}*, linewidths (full width at half maximum), and maximum extinctions of the resonance peaks closest to the laser wavelength (1060nm).*

Sample	Arm length (nm)	Λ (nm)	Polarisation	λ_{max}(nm)	FWHM (nm)	Extinction
1a	275	500	y	1093	105	1.03
1b	275	707	y	1156	79	0.61
1c	275	1000	y	1162	250	0.13
1d	275	707	y	1162	74	0.62
2a	250	500	v	1055	93	0.99
2b	250	707	v	1111	78	0.51
2c	250	1000	v	1086	242	0.11
2d	250	707	v	1099	79	0.49
3a	175	500	x	1042	91	0.82
3b	175	1000	x	1073	196	0.09
3c	175	707	x	1093	81	0.36
3d	180	731	x	1099	94	0.30

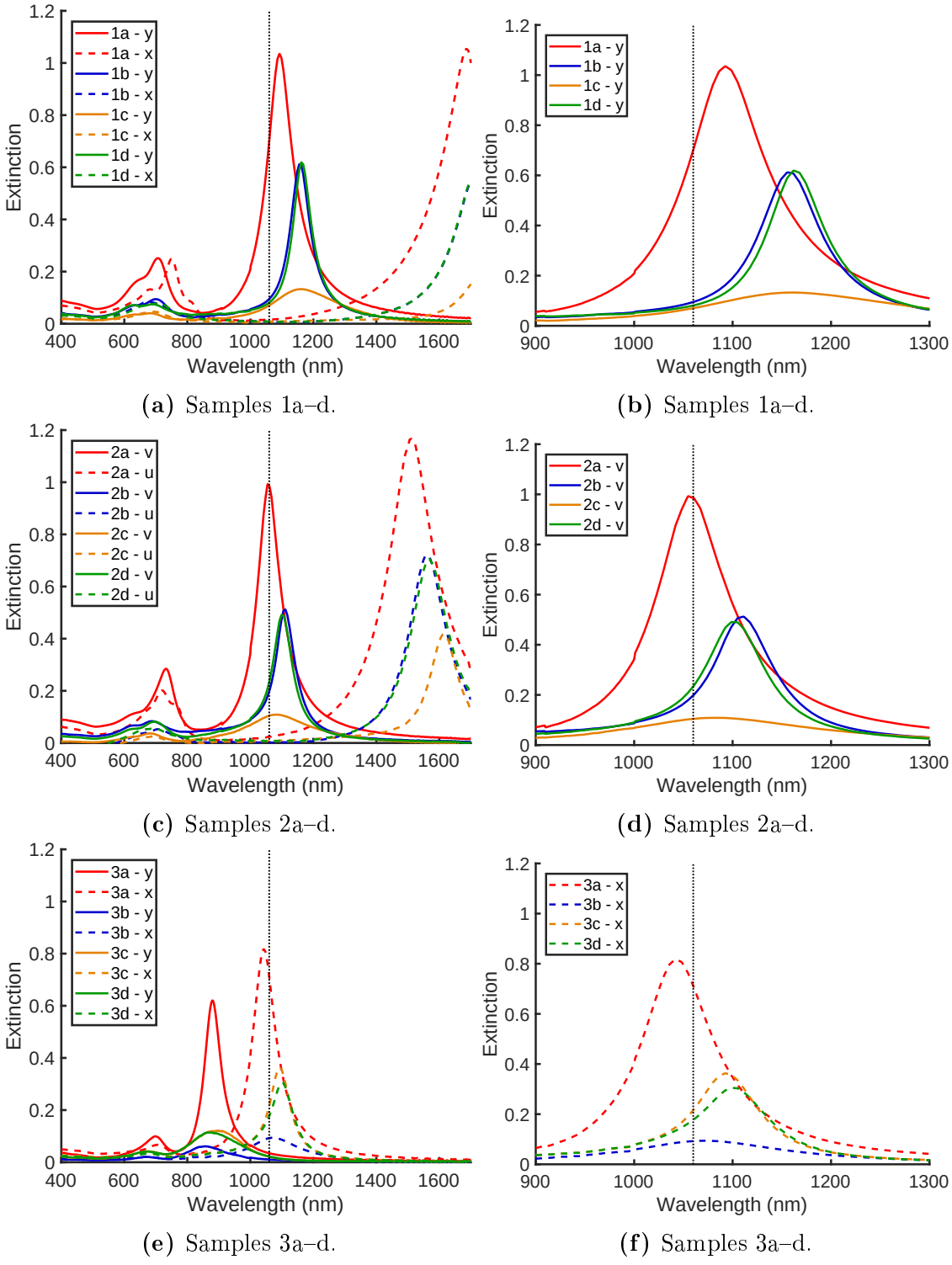

(a) Samples 1a–d.

(b) Samples 1a–d.

(c) Samples 2a–d.

(d) Samples 2a–d.

(e) Samples 3a–d.

(f) Samples 3a–d.

Figure 5.1 *Left column: measured extinction spectra. Right column: zoomed-in figures containing resonances near the laser wavelength for selected cases. Black dotted line marks the wavelength of the laser (1060nm).*

compared to Samples 2a–d, as is expected based on the longer arm length in Samples 1a–d. These resonances near the laser wavelength correspond to the fundamental resonance mode along the arms for particles with both 250 nm and 275 nm arm lengths, and therefore Samples 1a–d are expected to exhibit resonance-enhanced SHG with y-polarised fundamental field, and Samples 2a–d with v-polarised fundamental field.

Contrary to Samples 1a–d and 2a–d, a resonance with x-polarised light near the laser wavelength was observed for Samples 3a–3c and 3d with significantly shorter arm lengths of 175 nm and 180 nm, respectively. This resonance corresponds to oscillation over the whole L-shape, and these samples are expected to show resonance-enhanced SHG with x-polarised fundamental field. The differences between the spectra of Samples 3c and 3d are mostly explained by slightly increased arm length and array period. Increase in either quantity red-shifts the respective resonance, and increasing the array period leads to weaker resonance due to the decreased particle count. In addition to these differences, the resonance of Sample 3d has significantly larger linewidth.

A few observations can be made. Increasing the lattice constant leads to lower extinction at the resonance wavelength. This is expected, as increasing lattice constant (and, therefore, separation between the particles) leads to reducing the number of particles per surface area, which means there is less material interacting with light. Another observation is that the resonances of the samples with 707 nm lattice constants are narrower and red-shifted compared to samples with 500 nm lattice constant. This can be explained by the fact that samples with 707 nm lattice constant have a SLR mode near the observed resonance while 500 nm lattice samples do not (see Table 4.1). The presence of this SLR mode causes the red-shift of the resonance [19–21, 46].

A weak resonance near 700 nm wavelength was observed for all samples for both polarisations. This resonance is due to oscillations across the width of the arms [43], as evidenced by the fact that the resonance occurs for all samples (as the arm width is 100 nm for all samples) and for both polarisations. It is also possible that weak higher-order resonances of the particles modify the spectra in this region.

Another observation is that the spectra lack sharp features that result from incident light coupling to the SLR modes [20, 21, 27, 47]. While this result seems interesting at first glance, the smooth spectra likely result from the experimental setup used in linear measurements and specifically the microscope objectives used to focus the light onto the sample. The objectives have relatively large numerical apertures,

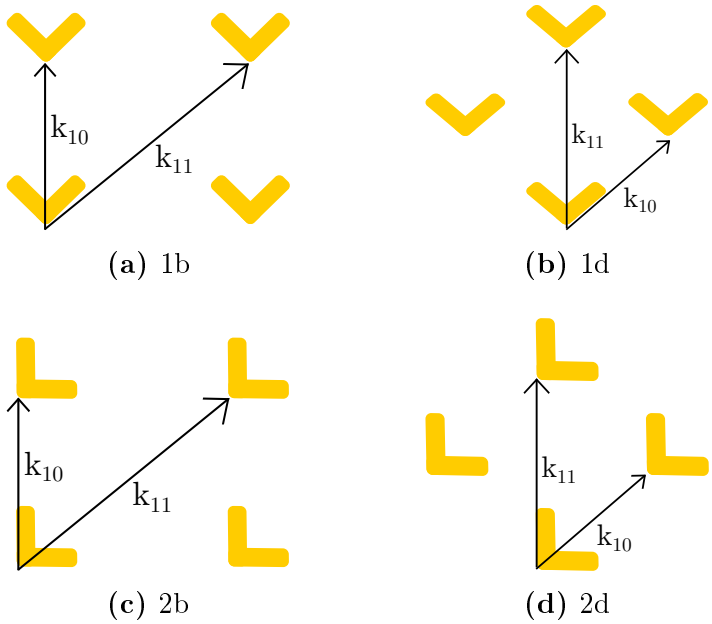

Figure 5.2 *Surface lattice resonance modes presents in Samples a) 1b, b) 1d, c) 2b, and d) 2d.*

which means light hits the sample at a large range of incident angles at the same time. As a result, the setup effectively averages the sample response over this range of angles of incidence, and since the surface lattice resonance wavelength depends on the angle of incidence [19, 21, 27], the expected sharp features resulting from lattice resonances cannot be discerned from the extinction spectra.

While the experimental setup hides most prominent spectral features of SLRs, the effects of the resonances can still be seen in other features of the spectra. This can be seen when comparing Samples 1b and 1d which have almost identical spectra. This is expected, as both samples have the same arm length and lattice constant, resulting in the same number of particles per surface area, and, therefore, are expected to have similar linear optical properties. However, the resonance of Sample 1d is red-shifted by a small margin compared to that of Sample 1b. Similar observation can be made for Samples 2b and 2d, where the resonance of Sample 2d is red-shifted compared to 2b. In both cases, this red-shift is accompanied by a small increase in the extinction at the centre wavelength of the resonance. Similar result has been reported previously by Tuovinen *et.al.* [48].

The difference in the resonance wavelength is likely arising from different orientations of the square lattices of the samples. In Samples 1b and 2b, the centre-to-centre distance between nanoparticles is 707 nm (equal to the lattice constant) in x- and y-directions, whereas in Samples 1d and 2d the particles the distance is in u- and v-directions, which are rotated by 45° from x- and y-directions, respectively. In

other words, the unit cells of the lattices of Samples 1b and 2b are rotated by 45° in comparison to those of Samples 1d and 2d, respectively. For these four samples, the fundamental surface lattice resonance mode is at 1025 nm (Table 4.1), which is near the observed resonances. However, as illustrated by Figures 5.2a and 5.2c, the fundamental mode k_{10} coincides with the x- and y-directions in Samples 1b and 2b, and with u- and v-direction for Samples 1d and 2d, as demonstrated by Figures 5.2b and 5.2d.

Now, the observed changes in the resonances of Samples 1d and 2b compared to 1b and 2d, respectively, suggest that the alignment of the lattice resonance modes with respect to the resonant polarisation direction of the plasmon resonance has an effect on the total response of the structure. Indeed, it has been shown that for square lattices, coupling of light to the SLR mode k_{10} is strongest in directions perpendicular to the polarisation and negligible in the directions parallel to the polarisation [25,49]. In comparison, rotated square arrays have been found to behave differently. Whenever the lattice mode is at 45° angle compared to the polarisation, light couples equally to the SLR mode k_{10} in all four directions [49].

Finally, a meaningful comparison can be made between Samples 1b and 2d, since their lattices are effectively the same, but in Sample 1b the arms of the nanoparticles are 25 nm longer. Samples 1d and 2b form a similar pair. This allows observing the effects of increased arm length of the particles. Figures 5.3a and 5.3b show the relevant spectra, which, along with the data in Table 5.1, show that an increase in the arm length of the particles red-shifts the resonance wavelength (as discussed earlier) and also increases the maximum extinction. However, the linewidth and the shape of the resonance peak seem to remain mostly unaffected.

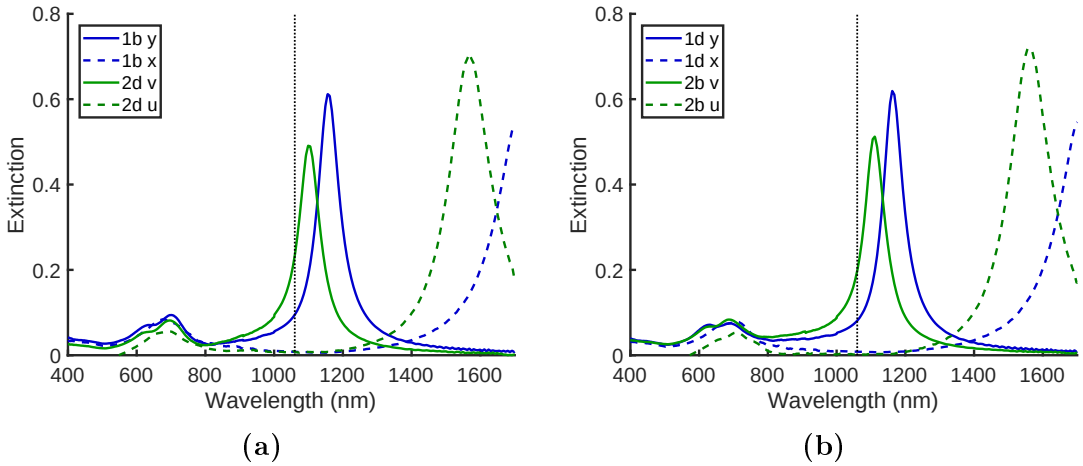

Figure 5.3 *Comparison between extinction spectra of Samples a) 1b and 2d, and b) 1d and 2b.*

5.2 Second-harmonic generation

As discussed in Chapter 4.4, the incident field components depend on the rotation angle θ of the half-wave plate HWP3 according to the relations

$$E_x(\omega) = E_0(\omega)\cos(2\theta) \tag{5.1}$$

$$E_y(\omega) = E_0(\omega)\sin(2\theta). \tag{5.2}$$

Substituting these fields into equation 3.11 yields

$$E_y(2\omega) = A_{yxx}E_0^2\cos^2(2\theta) + A_{yyy}E_0^2\sin^2(2\theta), \tag{5.3}$$

which means that it is possible to probe different nonlinear tensor components by rotating the wave plate. Since intensity is directly proportional to the square of the electric field, the generated SH field could be extracted from the measured intensities. However, since the focus of this work is in the response of the samples relative to each other, it is possible to include various constants in the nonlinear response tensor. This results in simplified equation

$$I_{2\omega}(\theta) = \left[A_{yxx}\cos^2(2\theta) + A_{yyy}\sin^2(2\theta)\right]^2 \tag{5.4}$$

which was the function used in the curve fitting process. For samples 2a-d, the relevant tensor components are A_{vuu} and A_{vvv}, and the fundamental fields were

$$E_v(\omega) = E_0(\omega)\cos(2\,(\theta + \pi/8)) \tag{5.5}$$

$$E_u(\omega) = E_0(\omega)\sin(2\,(\theta + \pi/8)) \tag{5.6}$$

and the function used in the fitting process was thus

$$I_{2\omega}(\theta) = \left[A_{vuu}\cos^2(2\,(\theta + \pi/8)) + A_{vvv}\sin^2(2\,(\theta + \pi/8))\right]^2. \tag{5.7}$$

An example of observed SHG and fitted curve is shown in Figure 5.4, and acquired values for relevant tensor components are presented in Table 5.2.

The quality of the fitted curves were checked both by R^2 coefficient and by eye. The model resulted in very high quality fits with a few exceptions (Samples 1c, 1d and 2c). These exceptions are due to the the weak nonlinear responses of these three samples, which results in low signal-to-noise ratio. However, comparing fitted curves to experimental data shows that fits capture intensity maxima acceptably, and thus comparing the maximum response of the samples can be done using the acquired values for the NRT components.

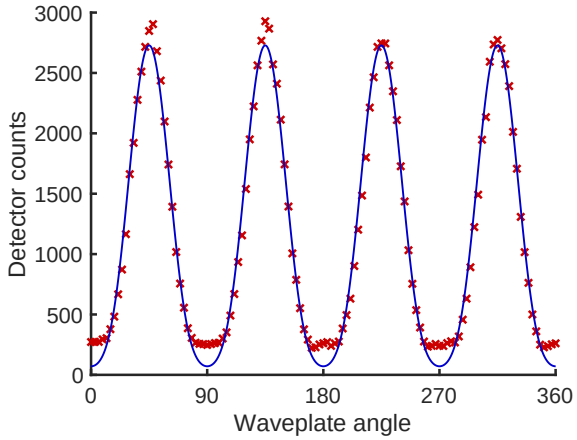

Figure 5.4 *Example of measured SHG for sample 1a (crosses), and the curve obtained from the fitting function (solid line).*

As predicted based on the measured extinction spectra, A_{yyy} was found to be the dominant component for Samples 1a–d, which exhibited plasmon resonance for y-polarised light near the laser wavelength (1060 nm). Similarly, for Samples 2a–d with v-polarised resonance near the laser wavelength, the A_{vvv} was found to dominate the response. A_{yxx} was found to be the dominant component for Samples 3a–d with resonance near the laser wavelength for x-polarised light. Therefore, it is evident that the observed SHG was resonantly enhanced for all samples.

Comparing the resonantly enhanced NRT components reveals that the observed SHG from Sample 3a was significantly stronger than SHG from any other sample. This is, however, at least partially explained by the fact that for SHG from L-

Table 5.2 *Nonlinear tensor components resulting from the fitting process. Bolded value indicates that component is resonantly enhanced. The fit functions are presented in equations 5.4 and 5.7.* Λ *is the lattice constant.*

Sample	Λ(nm)	A_{yxx} or A_{vuu}	A_{yyy} or A_{vvv}
1a	500	8.4 ± 1.1	$\mathbf{52.2 \pm 0.5}$
1b	707	-4.8 ± 0.5	$\mathbf{17.1 \pm 0.2}$
1c	1000	-3.6 ± 0.5	$\mathbf{8.0 \pm 0.2}$
1d	707	-6.4 ± 0.5	$\mathbf{13.2 \pm 0.3}$
2a	500	18.7 ± 0.6	$\mathbf{87.9 \pm 0.3}$
2b	707	-3.9 ± 0.7	$\mathbf{34.9 \pm 0.2}$
2c	1000	2.7 ± 0.4	$\mathbf{10.3 \pm 0.2}$
2d	707	-4.5 ± 2.0	$\mathbf{53.0 \pm 0.6}$
3a	500	$\mathbf{131.0 \pm 0.5}$	5.5 ± 1.6
3b	1000	$\mathbf{17.5 \pm 0.2}$	1.9 ± 0.5
3c	707	$\mathbf{86.2 \pm 0.7}$	-1.6 ± 2.5
3d	731	$\mathbf{38.2 \pm 0.2}$	1.5 ± 0.6

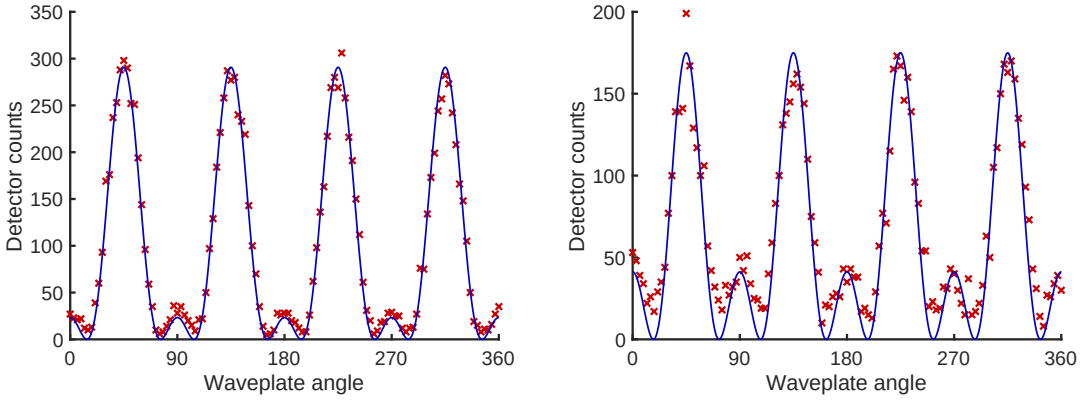

(a) Sample 1b **(b)** Sample 1d

Figure 5.5 *Samples 1b and 1d, for which tensor components A_{yyy} and A_{yxx} have opposite signs. Experimental data is represented by red crosses and the fit function by solid line. Note the different scaling of the vertical axes.*

nanoparticles, the highest power per solid angle propagates in normal (perpendicular to the xy-plane) direction when the fundamental field is in x-polarised (u-polarised for Samples 2a–d). In comparison, for y-polarised (v-polarised) fundamental field highest power per solid angle is radiated at an angle with respect to the normal direction [50]. This means that in the setup used for these measurements, a larger portion of the generated SH reaches the detector when the fundamental field is x-polarised (u-polarised) than when the fundamental field is y-polarised (v-polarised).

Another observation is that for Samples 1b, 1c and 1d, the non-dominant tensor component A_{yxx} has the opposite sign than A_{yyy} while being relatively large. As can be seen in Figures 5.5a and 5.5b, the nonlinear response shows a smaller local maximum between each two larger local maxima. These additional maxima with smaller peak value correspond to NRT component A_{yxx}, and the fact that the response goes to (near) zero between the maxima corresponding to different tensor components tells that the tensor components have opposite signs.

Now, it is a straightforward observation that the samples with lattice constant of 500 nm had the strongest nonlinear response for all particle sizes, whereas samples with 1000 nm lattice constant had the lowest response. This is expected, as increasing the size of the unit cell decreases the number density of particles, meaning that there are fewer particles interacting with light. Ignoring the effects of the plasmon resonances, equation 3.7 suggests that the second-order nonlinear susceptibility should be directly proportional to the number of particles per surface area, so a decrease in the nonlinear response with decreased particle count is expected. However, the nonlinear tensor components in samples with 1000 nm lattice constant are significantly smaller than the decrease in particle count suggests.

Furthermore, comparing Sample pairs 1b and 1d, and 2b and 2d shows that, despite the samples having exactly the same particle sizes and lattice constants, their resonant NRT components have significantly different values. Additionally, comparison between the nonlinear responses of Samples 3c and 3d also indicates there being more factors in play, as the difference in number density is less than ten percent, but the resonant NRT component is different approximately by a factor of two.

Clearly, the differences in number densities alone cannot explain the differences in the nonlinear responses, and therefore there must be other factors in play. One such effect is the resonance enhancement (Chapter 3.5), where the plasmon resonance near the fundamental wavelength enhances the nonlinear response. A simple model for the effect of resonance enhancement can be obtained using the nonlinear Lorentz model (equation 3.7), which implies that the nonlinear response tensor components A_{yyy}, A_{vvv} and A_{yxx} should follow relation

$$A_{ijj} \propto R = \frac{N}{\left|D_j^2(\omega)\right|} = \frac{N}{\left|\left(\omega_j^2 - \omega^2 - 2i\omega\gamma_j\right)^2\right|} \approx \frac{1}{4\omega^2}\frac{N}{\left|\left(\Delta_j - i\gamma_j\right)^2\right|}, \tag{5.8}$$

where R denotes the resonance enhancement factor, N is the number density of particles, ω_j and ω are the resonance and laser frequencies, respectively, $\Delta_j = \omega_j - \omega$ is the detuning of the laser frequency from the resonance, and γ_j is equal to the half width at half maximum (HWHM) of the resonance. Subscripts i and j refer to the polarisations of the SH and the fundamental field, respectively. The approximation $\omega_j^2 - \omega^2 \approx 2\omega(\omega_j - \omega)$ is valid when the laser frequency is close to the resonance.

Table 5.3 *Comparison between the predicted resonance enhancement factors and determined tensor components. Number densities N, calculated enhancement factors R, and the resonant tensor components A_{ijj} of sample sets 1, 2, and 3 are normalised to Samples 1a, 2a, and 3a, respectively.*

Sample	Λ(nm)	N	Detuning (nm)	HWHM (nm)	R	A_{ijj}
1a	500	1	33	53	1	1
1b	707	0.5	96	40	0.20	0.33
1c	1000	0.25	102	125	0.04	0.15
1d	707	0.5	102	37	0.18	0.25
2a	500	1	5	47	1	1
2b	707	0.5	51	39	0.31	0.40
2c	1000	.25	26	121	0.04	0.12
2d	707	0.5	39	40	0.40	0.60
3a	500	1	18	46	1	1
3b	1000	0.25	13	98	0.07	0.13
3c	707	0.5	33	41	0.52	0.66
3d	731	0.47	39	47	0.36	0.29

The equation 5.8 was used to calculate the expected enhancement factors for all samples. The normalised values for these enhancement factors, as well as the NRT components determined from the experimental data, are presented in Table 5.3. Comparing the values of the expected enhancement factors and nonlinear tensor components shows that the model offers a decent prediction of the observed SHG. The predicted enhancement is of the same order of magnitude as the NRT components obtained from the experimental data, and the relative magnitudes are off by less than a factor of two, with two exceptions (Samples 1c and 2c). However, the agreement is not perfect, which could result from a few factors.

One and very possibly the most important factor is that, as discussed in Chapter 5.1, it is likely that the measured extinction spectra are not accurate and lack features resulting from SLRs. This would mean that the calculated enhancement factors are not accurate for samples that support SLRs. Indeed, a SLR mode at slightly shorter wavelength compared to the centre wavelength of the plasmon resonance often leads to narrower resonance [21, 27]. Therefore it is highly likely that the calculated enhancement factors are too small for samples that support SLR modes near the plasmon resonance (Samples 1b, 1d, 2b, 2d, 3c, and 3d).

Another factor is the possibility of nonlinear scaling of SLRs when the structures are subjected to a strong electric field. While the linear contribution of the SLRs on the extinction is (or rather, should be) included in the resonance enhancement, the observed differences in the nonlinear responses were larger than predicted based on the resonance enhancement factor alone. Again, the most likely reason for this is the inaccuracy of the measured extinction spectra, but some differences could result from nonlinearity of the SLRs appearing with strong fundamental field.

While the problems in determining extinction spectra and, therefore, resonance enhancement factors accurately prevents making definite conclusions about the effects of surface lattice resonances, the effects of lattice resonances can be seen in the determined nonlinear response tensor components. As discussed earlier, the differences in the nonlinear responses between samples cannot be explained by differences in the number density of particles, so they must arise from lattice effects.

Evidence for the importance of SLRs can be seen clearly from comparison between Samples 1b and 1d, and between 2b and 2d. Of these two pairs, higher nonlinear response was observed from Samples 1b and 2d, for which the detuning of the laser frequency from the resonance was smaller. This likely explains most of the difference. Furthermore, it is possible that the real resonances were narrower than the measured extinction spectra imply, which would result in further resonance enhancement.

Another possible explanation for the difference in the nonlinear responses in the aforementioned two sample pairs can be found in the coupling of fields to the SLRs. As discussed in Chapter 5.1, there is a distinct difference between differently ordered lattices. This was explained with how the SLR modes are aligned with respect to the resonant polarisations, and similar effect could affect the nonlinear responses.

It is also worthwhile to note that the nonlinear responses of Samples 3c and 3d also differ by more than the differences in particle density or resonance enhancement predict. There is a SLR mode at 1025 nm present in Sample 3c, but in Sample 3d, the resonance occurs at the wavelength of 1060 nm, which is exactly the laser wavelength. It is possible that this difference is at least partially due to the diffraction anomaly typically observed at the wavelength of the SLR mode [23, 26, 27], but again, the problems in determining extinction spectra accurately prevent from making a definite conclusion.

Some additional insight into the importance of both plasmon resonances and SLRs can be gained by comparing the strength of the nonlinear response to the amount of interacting material in the structures. In order to perform this comparison, the NRT components need to be scaled accordingly to the area of the sample covered by the particles.

Let us start by noting that for a sample in which the particles are arranged in a square array with lattice constant Λ, any square with area equal to Λ^2 should contain exactly one particle. If each particle has an area S, the ratio of the total area of the particles to the total area of the sample is equal to S/Λ^2. Dividing the experimentally obtained NRT components A_{ijj} with this ratio results in the equation

$$A'_{ijj} = \frac{\Lambda^2}{S} A_{ijj}, \tag{5.9}$$

where A'_{ijj} is the NRT component scaled to the relative area covered by the particles on the sample. To calculate the area of a single particle, the particle was assumed to consist of two touching rectangles like shown in Figure 5.6. Therefore, the area of a single particle is

$$S = lw + (l - w)w = 2lw - w^2, \tag{5.10}$$

where l is the arm length and w the arm width of the particle.

For this comparison, only NRT components corresponding to resonantly enhanced SHG are considered, as they are responsible for most of the observed SHG. These components are A_{yyy} for Samples 1a–d, A_{vvv} for Samples 2a–d, and A_{yxx} for Samples 3a–d. This comparison can be made because the experimental conditions, most

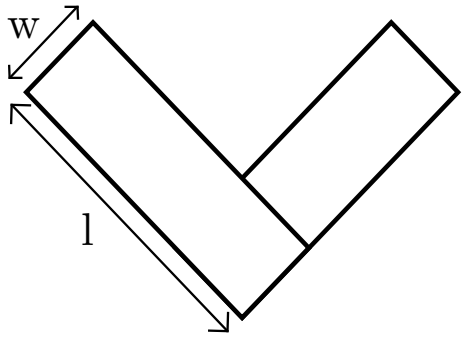

Figure 5.6 *The shape used for calculating the area of a single particle with the arm length l and the arm width w.*

importantly the beam diameter and the incident power at the sample, were kept constant for all samples. The normalised values for both experimentally obtained and scaled NRT components, as well as the values for Λ and l, for all samples are presented in Table 5.4. The arm width was 100 nm for all samples. The immediate observation is that while Sample 3a had the strongest measured nonlinear response, the strongest scaled response belongs to Sample 3c. In general, Samples 3a–d exhibited stronger scaled SHG than other samples.

Larger values of the scaled NRT components for Samples 3a–d are mostly explainable by two factors. First of all, as discussed earlier, larger portion of SHG is detected from x-resonant particles [50]. Another reason is that the particles are much smaller, which results in larger scaling factors and thus higher scaled values of the NRT

Table 5.4 *Comparison between the SHG generation per particle area for different samples. The lattice constants Λ and the arm lengths of the particles l were used for scaling the NRT components using equation 5.9. Both the scaled and experimentally obtained NRT components A'_{ijj} and A_{ijj}, respectively, are normalised to Sample 3a, and the largest values for both are* ***bolded****.*

Sample	Λ (nm)	l (nm)	A_{ijj}	A'_{ijj}
1a	500	275	0.40	0.22
1b	707	275	0.13	0.14
1c	1000	275	0.06	0.14
1d	707	275	0.10	0.11
2a	500	250	0.67	0.42
2b	707	250	0.27	0.33
2c	1000	250	0.08	0.20
2d	707	250	0.41	0.51
3a	500	175	**1.00**	1.00
3b	1000	175	0.13	0.53
3c	707	175	0.66	**1.32**
3d	731	180	0.29	0.60

components A'_{yxx}. This result highlights the importance of resonance enhancement in tuning nonlinear processes, as stronger response was achieved with less interacting material.

Comparing the scaled NRT components for Samples 1a–d reveals that they are rather close to each other. The scaled response of Sample 1a was the highest in this set, while Samples 1b–d differed very little from each other. This is likely due to large detuning of the resonance for Samples 1b–d, which leads to relatively weak resonance enhancement. Again, this result highlights the importance of resonances in the nonlinear response of nanostructures.

In contrast to Samples 1a–d, the scaled NRT components for Samples 2a–d are vary significantly more. This likely results from the fact that the laser wavelength is much closer to the resonances for all samples, and therefore differences in the shapes of the resonances have larger impact. A very important detail here is that the scaled nonlinear response of Sample 2d was higher than that of Sample 2a. This is a clear indication that the SLR present in Sample 2d enhances the resonance, which leads to stronger SHG. In a similar fashion, Sample 3c also shows the importance of SLRs when comparing the scaled NRT components of Samples 3a and 3c.

6. CONCLUSIONS

In this work, optical properties of nanostructures consisting of L-shaped gold nanoparticles in regular square lattices were studied. The size, orientation, and lattice dimensions were varied between different structures to study the effect of different parameters, with emphasis on SLRs. The studied properties were the extinction spectra and SHG of the structures.

The results for the extinction spectra were mixed. As expected, all structures were dichroic and exhibited a single strong and relatively narrow plasmon resonance for each polarisation. Some expected effects of SLRs were observed, but sharp spectral features associated with SLRs were not. The likely cause for the lack of these sharp features at the resonance wavelengths was deemed to be the used extinction setup and specifically the use of microscope objectives to focus the light onto the samples. The large numerical apertures of the objectives effectively average the spectra over a range of incident angles which, as the wavelengths of the SLR modes depend on the incident angle, hides these near-discrete resonances.

Despite the problems with the extinction setup, it was observed that a SLR mode at slightly shorter wavelength than the plasmon resonance of the nanoparticles modifies the total resonance of the structure by red-shifting and narrowing the resonance. This effect is interesting, since controlling the width and centre wavelength of the resonance allows for better tuning of the properties of the structure.

One example for which a narrower resonance is beneficial is SHG, where narrower resonance leads to stronger response via increased resonance enhancement. SHG from the structures was measured and analysis revealed that for each sample, the observed SHG had strong dependence on the polarisation of the fundamental field, as was expected from the strong dichroism of the structures. Furthermore, the polarisation that produced the highest SH intensity coincided with the polarisation at which the resonance of the structure was closest to the laser wavelength. This leads to the conclusion that the SHG from the structures was resonantly enhanced for certain fundamental field polarisations.

To explain the effect of the resonance enhancement, a nonlinear Lorentz model was used to calculate the expected enhancement factors based on the measured extinction spectra. The model provided a decent estimate of the observed differences in SHG, but the agreement was not perfect. The inaccuracy of the predictions provided by the model can largely be attributed to the the problems in determining the extinction spectra, since the real resonances at normal incidence could be significantly narrower than the experimental data suggested.

While the model for resonance enhancement proved to be inadequate for fully explaining the nonlinear responses, evidence of surface lattice resonances enhancing SHG could be seen in the results. Structures that supported SLR modes near the laser wavelength had stronger SHG response relative to the number of particles per surface area when compared to structures with no such SLR modes. Additionally, a clear difference in SHG was observed between structures with same number of particles per surface area but different lattice order. Furthermore, comparing the observed SHG to the relative area of the particles showed clear differences between differently sized particles and lattices, which provided further evidence on the importance of resonances.

In conclusion, the results presented in this work clearly show that surface lattice resonances affect both linear and nonlinear responses of periodic gold nanostructures. This is a promising result, and especially the differences observed between lattices with equal periods but differently oriented lattice modes are worth studying further, possibly using oblique angles of incidence. Additionally, a SHG setup incorporating a tunable laser could be used to better characterise the resonance enhancement of the nanostructures. However, the suspected problems with the extinction setup meant that some questions were left unanswered, and in future studies care should be taken to ensure proper collimation of light used to probe the structures.

BIBLIOGRAPHY

[1] R. W. Boyd, *Nonlinear Optics*, 2nd ed. San Diego: Academic Press, 2003.

[2] S. A. Maier, *Plasmonics: Fundamentals and Applications*, 1st ed. New York: Springer Verlag, 2007.

[3] N. Fang, H. Lee, C. Sun, and X. Zhang, "Sub–diffraction-limited optical imaging with a silver superlens," *Science*, vol. 308, no. 5721, pp. 534–537, 2005.

[4] J. Aizpurua, P. Hanarp, D. S. Sutherland, M. Käll, G. W. Bryant, and F. J. García de Abajo, "Optical properties of gold nanorings," *Phys. Rev. Lett.*, vol. 90, p. 057401, Feb 2003.

[5] K. L. Kelly, E. Coronado, L. L. Zhao, and G. C. Schatz, "The optical properties of metal nanoparticles: The influence of size, shape, and dielectric environment," *J. Phys. Chem. B*, vol. 107, no. 3, pp. 668–677, 2003.

[6] B. K. Canfield, S. Kujala, K. Jefimovs, J. Turunen, and M. Kauranen, "Linear and nonlinear optical responses influenced by broken symmetry in an array of gold nanoparticles," *Opt. Express*, vol. 12, no. 22, pp. 5418–5423, Nov 2004.

[7] K.-S. Lee and M. A. El-Sayed, "Dependence of the enhanced optical scattering efficiency relative to that of absorption for gold metal nanorods on aspect ratio, size, end-cap shape, and medium refractive index," *J. Phys. Chem. B*, vol. 109, no. 43, pp. 20 331–20 338, 2005.

[8] S. S. Shankar, A. Rai, A. Ahmad, and M. Sastry, "Controlling the optical properties of lemongrass extract synthesized gold nanotriangles and potential application in infrared-absorbing optical coatings," *Chem. Mater.*, vol. 17, no. 3, pp. 566–572, 2005.

[9] A. Sundaramurthy, K. B. Crozier, G. S. Kino, D. P. Fromm, P. J. Schuck, and W. E. Moerner, "Field enhancement and gap-dependent resonance in a system of two opposing tip-to-tip au nanotriangles," *Phys. Rev. B*, vol. 72, p. 165409, Oct 2005.

[10] M. W. Klein, C. Enkrich, M. Wegener, and S. Linden, "Second-harmonic generation from magnetic metamaterials," *Science*, vol. 313, no. 5786, pp. 502–504, 2006.

[11] C. Rockstuhl, T. Zentgraf, H. Guo, N. Liu, C. Etrich, I. Loa, K. Syassen, J. Kuhl, F. Lederer, and H. Giessen, "Resonances of split-ring resonator metamaterials in the near infrared," *Appl. Phys. B*, vol. 84, no. 1, pp. 219–227, Jul 2006.

[12] M. W. Klein, M. Wegener, N. Feth, and S. Linden, "Experiments on second- and third-harmonic generation from magnetic metamaterials," *Opt. Express*, vol. 15, no. 8, pp. 5238–5247, Apr 2007.

[13] M. Sukharev, J. Sung, K. G. Spears, and T. Seideman, "Optical properties of metal nanoparticles with no center of inversion symmetry: Observation of volume plasmons," *Phys. Rev. B*, vol. 76, p. 184302, Nov 2007.

[14] F. Hao, E. M. Larsson, T. A. Ali, D. S. Sutherland, and P. Nordlander, "Shedding light on dark plasmons in gold nanorings," *Chem. Phys. Lett.*, vol. 458, no. 4, pp. 262 – 266, 2008.

[15] E. Tatartschuk, E. Shamonina, and L. Solymar, "Plasmonic excitations in metallic nanoparticles: Resonances, dispersion characteristics and near-field patterns," *Opt. Express*, vol. 17, no. 10, pp. 8447–8460, May 2009.

[16] B. Lamprecht, G. Schider, R. T. Lechner, H. Ditlbacher, J. R. Krenn, A. Leitner, and F. R. Aussenegg, "Metal nanoparticle gratings: Influence of dipolar particle interaction on the plasmon resonance," *Phys. Rev. Lett.*, vol. 84, pp. 4721–4724, May 2000.

[17] W. Rechberger, A. Hohenau, A. Leitner, J. Krenn, B. Lamprecht, and F. Aussenegg, "Optical properties of two interacting gold nanoparticles," *Opt. Comm.*, vol. 220, no. 1, pp. 137 – 141, 2003.

[18] S. Zou, N. Janel, and G. C. Schatz, "Silver nanoparticle array structures that produce remarkably narrow plasmon lineshapes," *J. Chem. Phys.*, vol. 120, no. 23, pp. 10 871–10 875, 2004.

[19] N. Félidj, G. Laurent, J. Aubard, G. Lévi, A. Hohenau, J. R. Krenn, and F. R. Aussenegg, "Grating-induced plasmon mode in gold nanoparticle arrays," *J. Chem. Phys.*, vol. 123, no. 22, p. 221103, 2005.

[20] B. Auguié and W. L. Barnes, "Collective resonances in gold nanoparticle arrays," *Phys. Rev. Lett.*, vol. 101, p. 143902, Sep 2008.

[21] Y. Chu, E. Schonbrun, T. Yang, and K. B. Crozier, "Experimental observation of narrow surface plasmon resonances in gold nanoparticle arrays," *Appl. Phys. Lett.*, vol. 93, no. 18, p. 181108, 2008.

[22] V. G. Kravets, F. Schedin, and A. N. Grigorenko, "Extremely narrow plasmon resonances based on diffraction coupling of localized plasmons in arrays of metallic nanoparticles," *Phys. Rev. Lett.*, vol. 101, p. 087403, Aug 2008.

[23] R. Adato, A. A. Yanik, C.-H. Wu, G. Shvets, and H. Altug, "Radiative engineering of plasmon lifetimes in embedded nanoantenna arrays," *Opt. Express*, vol. 18, no. 5, pp. 4526–4537, Mar 2010.

[24] C. Ciracì, E. Poutrina, M. Scalora, and D. R. Smith, "Second-harmonic generation in metallic nanoparticles: Clarification of the role of the surface," *Phys. Rev. B*, vol. 86, p. 115451, Sep 2012.

[25] A. D. Humphrey and W. L. Barnes, "Plasmonic surface lattice resonances on arrays of different lattice symmetry," *Phys. Rev. B*, vol. 90, p. 075404, Aug 2014.

[26] M. Kataja, T. Hakala, A. Julku, M. Huttunen, S. van Dijken, and P. Törmä, "Surface lattice resonances and magneto-optical response in magnetic nanoparticle arrays," *Nat. Commun.*, vol. 6, 2015.

[27] R. Czaplicki, A. Kiviniemi, J. Laukkanen, J. Lehtolahti, M. Kuittinen, and M. Kauranen, "Surface lattice resonances in second-harmonic generation from metasurfaces," *Opt. Lett.*, vol. 41, no. 12, pp. 2684–2687, Jun 2016.

[28] J. C. Maxwell, "A dynamical theory of the electromagnetic field," *Phil. Trans.*, vol. 155, pp. 459–512, 1865.

[29] E. Hecht, *Optics*, 4th ed. San Francisco: Addison Wesley, 2002.

[30] M. Mansfield and C. O'Sullivan, *Understanding Physics*, 2nd ed. Chichester: Wiley, 2011.

[31] H. A. Lorentz, *The Theory of Electrons and Its Applications to the Phenomena of Light and Radiant Heat*, 2nd ed. New York: Dover Publications Inc., 1952.

[32] B. K. Canfield, S. Kujala, K. Jefimovs, T. Vallius, J. Turunen, and M. Kauranen, "Polarization effects in the linear and nonlinear optical responses of gold nanoparticle arrays," *J. Opt. A*, vol. 7, no. 2, p. S110, 2005.

[33] S. Kujala, B. K. Canfield, M. Kauranen, Y. Svirko, and J. Turunen, "Multipolar analysis of second-harmonic radiation from gold nanoparticles," *Opt. Express*, vol. 16, no. 22, pp. 17 196–17 208, Oct 2008.

[34] J. Valentine, S. Zhang, T. Zentgraf, E. Ulin-Avila, D. A. Genov, G. Bartal, and X. Zhang, "Three-dimensional optical metamaterial with a negative refractive index," *Nature*, vol. 455, no. 7211, pp. 376–379, 2008.

[35] M. Pelton and G. Bryant, *Introduction to Metal-Nanoparticle Plasmonics*, ser. A Wiley-Science Wise Co-Publication. New York: Wiley, 2013.

[36] P. L. Stiles, J. A. Dieringer, N. C. Shah, and R. P. V. Duyne, "Surface-enhanced raman spectroscopy," *Annu. Rev. Anal. Chem.*, vol. 1, no. 1, pp. 601–626, 2008.

[37] C. Gabrielli and H. Perrot, *Modern Aspects of Electrochemistry: Modeling and Numerical Simulations II.* New York: Springer, 2009.

[38] R. Czaplicki, J. Mäkitalo, R. Siikanen, H. Husu, J. Lehtolahti, M. Kuittinen, and M. Kauranen, "Second-harmonic generation from metal nanoparticles: Resonance enhancement versus particle geometry," *Nano Lett.*, vol. 15, no. 1, pp. 530–534, 2015.

[39] B. K. Canfield, S. Kujala, K. Jefimovs, Y. Svirko, J. Turunen, and M. Kauranen, "A macroscopic formalism to describe the second-order nonlinear optical response of nanostructures," *J. Opt. A*, vol. 8, no. 4, p. S278, 2006.

[40] F. B. P. Niesler, N. Feth, S. Linden, and M. Wegener, "Second-harmonic optical spectroscopy on split-ring-resonator arrays," *Opt. Lett.*, vol. 36, no. 9, pp. 1533–1535, May 2011.

[41] M. Meier, A. Wokaun, and P. F. Liao, "Enhanced fields on rough surfaces: dipolar interactions among particles of sizes exceeding the rayleigh limit," *J. Opt. Soc. Am. B*, vol. 2, no. 6, pp. 931–949, Jun 1985.

[42] U. Fano, "Effects of configuration interaction on intensities and phase shifts," *Phys. Rev.*, vol. 124, pp. 1866–1878, Dec 1961.

[43] H. Husu, J. Mäkitalo, J. Laukkanen, M. Kuittinen, and M. Kauranen, "Particle plasmon resonances in L-shaped gold nanoparticles," *Opt. Express*, vol. 18, no. 16, pp. 16 601–16 606, Aug 2010.

[44] B. K. Canfield, S. Kujala, K. Laiho, K. Jefimovs, J. Turunen, and M. Kauranen, "Chirality arising from small defects in gold nanoparticle arrays," *Opt. Express*, vol. 14, no. 2, pp. 950–955, Jan 2006.

[45] H. Husu, J. Mäkitalo, R. Siikanen, G. Genty, H. Pietarinen, J. Lehtolahti, J. Laukkanen, M. Kuittinen, and M. Kauranen, "Spectral control in anisotropic resonance-domain metamaterials," *Opt. Lett.*, vol. 36, no. 12, pp. 2375–2377, Jun 2011.

[46] M. Decker, N. Feth, C. M. Soukoulis, S. Linden, and M. Wegener, "Retarded long-range interaction in split-ring-resonator square arrays," *Phys. Rev. B*, vol. 84, p. 085416, Aug 2011.

[47] A. I. Väkeväinen, R. J. Moerland, H. T. Rekola, A.-P. Eskelinen, J.-P. Martikainen, D.-H. Kim, and P. Törmä, "Plasmonic surface lattice resonances at the strong coupling regime," *Nano Lett.*, vol. 14, no. 4, pp. 1721–1727, 2014.

[48] H. Tuovinen, M. Kauranen, K. Jefimovs, P. Vahimaa, T. Vallius, J. Turunen, N. V. Tkachenko, and H. Lemmetyinen, "Linear and second-order nonlinear optical properties of arrays of noncentrosymmetric gold nanoparticles," *J. Nonlinear Opt. Phys. Mater.*, vol. 11, no. 04, pp. 421–432, 2002.

[49] R. Guo, T. K. Hakala, and P. Törmä, "Geometry dependence of surface lattice resonances in plasmonic nanoparticle arrays," *Phys. Rev. B*, vol. 95, p. 155423, Apr 2017.

[50] J. Mäkitalo, S. Suuriniemi, and M. Kauranen, "Boundary element method for surface nonlinear optics of nanoparticles," *Opt. Express*, vol. 19, no. 23, pp. 23 386–23 399, Nov 2011.